

Keck Absorption-Line Spectroscopy of Galactic Winds in Ultraluminous Infrared Galaxies

David S. Rupke^{1,2}, Sylvain Veilleux^{1,2,3}, and D. B. Sanders^{2,4}

ABSTRACT

In this paper, we present moderately-high resolution ($\sim 65 \text{ km s}^{-1}$) spectroscopy, acquired with ESI on Keck II, of 11 ultraluminous infrared galaxies at $z < 0.3$ from the IRAS 1 Jy sample. The targets were chosen as good candidates to host galaxy-scale outflows, and most have infrared luminosities dominated by star formation. We use a χ^2 minimization to fit one- to three-component profiles to the Na I D interstellar absorption doublet in each object. Assuming that gas blueshifted by more than 70 km s^{-1} relative to the systemic velocity of the host is outflowing, we detect outflows in 73% of these objects. We adopt a simple model of a mass-conserving free wind to infer mass outflow rates in the range $\dot{M}_{\text{tot}}(\text{H}) = 13 - 133 M_{\odot} \text{ yr}^{-1}$ for galaxies hosting a wind. These values of \dot{M}_{tot} , normalized to the corresponding global star formation rates inferred from infrared luminosities, are in the range $\eta \equiv \dot{M}_{\text{tot}}/\text{SFR} = 0.1 - 0.7$. This is on average a factor of only 10 less than η from recent measurements of nearby dwarfs, edge-on spirals, and lower-luminosity infrared galaxies. Within our sample, we conclude that η has no dependence on the mass of the host (parameterized by host galaxy kinematics and absolute R - and K' -band magnitudes). We also attempt to estimate the average escape fraction $\langle f_{\text{esc}} \rangle \equiv \sum \dot{M}_{\text{esc}}^i / \sum \dot{M}_{\text{tot}}^i$ and “ejection efficiency” $\langle \delta \rangle \equiv \sum \dot{M}_{\text{esc}}^i / \sum \text{SFR}^i$ for our sample, which we find to be $\sim 0.4 - 0.5$ and ~ 0.1 , respectively. The complex absorption-line properties of Mrk 231, an ultraluminous infrared galaxy which is optically classified as a Seyfert 1, are discussed separately in an appendix.

¹Department of Astronomy, University of Maryland, College Park, MD 20742; drupke@astro.umd.edu, veilleux@astro.umd.edu

²Guest observers at the W.M. Keck Observatory, which is operated as a scientific partnership among the California Institute of Technology, the University of California and the National Aeronautics and Space Administration. The Observatory was made possible by the generous financial support of the W.M. Keck Foundation.

³Cottrell Scholar of Research Corporation

⁴Institute for Astronomy, University of Hawaii, 2680 Woodlawn Drive, Honolulu, HI 96822; sanders@ifa.hawaii.edu

Subject headings: galaxies: starburst — galaxies: active — galaxies: evolution
 — ISM: jets and outflows — ISM: kinematics and dynamics

1. INTRODUCTION

Large-scale galactic outflows, energized by stellar winds and supernovae ejecta or a central AGN, are ubiquitous in the local universe and at high redshift (Pettini et al. 2001; Frye, Broadhurst, & Benítez 2002). Theoretical work, both analytical and numerical, suggests that these outflows may be important in galaxy formation (e.g. Dekel & Silk 1986; Scannapieco, Ferrara, & Broadhurst 2000; Scannapieco & Broadhurst 2001; Scannapieco, Thacker, & Davis 2001). They also play a role in galactic evolutionary processes, especially the regulation of star formation by mechanical feedback (e.g. Oey, Clarke, & Massey 2001) and the enrichment of galactic halos. The expulsion of metals from galaxies by galactic winds may be able to reproduce the color-magnitude (or mass-metallicity) relation of ellipticals, since more massive galaxies, with larger gravitational potentials, could retain mass and metals more easily in this scenario (Larson 1974; Vader 1986; Franx & Illingworth 1990; Kauffmann & Charlot 1998). Besides their impact on individual galaxies, galactic winds may contribute significantly to the chemical and thermal evolution of the universe by enriching and heating the intergalactic medium (e.g. Nath & Trentham 1997; Aguirre et al. 2001; Madau, Ferrara, & Rees 2001), which is known to contain substantial amounts of metals even at high redshift and low density (e.g. Cowie & Songaila 1998). Winds are also a possible mechanism for the preheating and enrichment of the intracluster medium in groups and clusters of galaxies (e.g. David, Forman, & Jones 1991; Ponman, Cannon, & Navarro 1999). Finally, these outflows could be responsible for the damped Ly α or strong Mg II absorption systems observed in quasar spectra (e.g. Efstathiou 2000; Chen et al. 2001; Bond et al. 2001), and may contribute to reionization by opening a path for Lyman continuum photons to escape star-forming regions (Madau, Haardt, & Rees 1999; Dove, Shull, & Ferrara 1999; Steidel, Pettini, & Adelberger 2001; Pettini et al. 2001).

The observational dataset on galactic-scale outflows is slim, however, apart from studies of the local universe ($z < 0.1$) and high-redshift galaxies [Lyman-break galaxies at $z \sim 3$ (Pettini et al. 2000, 2001) and a few gravitationally-lensed objects (Frye et al. 2002)]. In this paper, we present and discuss the results of a moderately-high resolution ($R \sim 4600$, or $\Delta v \sim 65 \text{ km s}^{-1}$) spectroscopic study of winds in ultraluminous infrared galaxies (ULIGs) with redshifts of $0.04 < z < 0.27$. ULIGs, which by definition have $L_{\text{IR}} > 10^{12} L_{\odot}^5$, contain

⁵ $L_{\text{IR}} = L(8 - 1000) \mu\text{m}$, computed using the single-temperature dust-emissivity fit to all four IRAS flux

massive starbursts and/or AGN (Veilleux, Sanders, & Kim 1999b; Lutz, Veilleux, & Genzel 1999), and have been associated with large-scale outflows at low redshift (e.g. Heckman, Armus, & Miley 1990; Kim, Veilleux, & Sanders 1998). ULIGs, especially those whose energy output is dominated by stars, are important sites of obscured star formation at low z (Sanders & Mirabel 1996). There are suggestions from infrared and submillimeter counts that there is a strong increase in the number density of ULIGs with z (IRAS: Kim & Sanders 1998; ISO: Kawara et al. 1998; Puget et al. 1999; Matsuhara et al. 2000; Efstathiou et al. 2000; Serjeant et al. 2001; SCUBA: Smail, Ivison, & Blain 1997; Hughes et al. 1998; Blain et al. 1999; Eales et al. 1999; Barger, Cowie, & Sanders 1999), implying that ULIGs contain a substantial fraction of high- z star formation (although this is not necessarily true; see Trentham, Blain, & Goldader 1999). ULIGs may also be a highly reddened and luminous subset of the UV-selected Lyman-break galaxies (e.g. Sanders 1999; Trentham et al. 1999), which typically produce outflows (Pettini et al. 2001).

Absorption-line spectroscopy has proven to be an effective method for probing various phases of the ISM at low and high redshift: the warm neutral ($T \lesssim 10^4$ K) component, using Na I D [Phillips 1993 (NGC 1808); Heckman et al. 2000]; the warm ionized ($T \sim 10^{4-5}$ K) component, using UV lines [Lequeux et al. 1995 (Mrk 33); Heckman & Leitherer 1997 (NGC 1705); Sahu & Blades 1997 (NGC 1705); Kunth et al. 1998; González Delgado et al. 1998; Pettini et al. 2001]; and the hot coronal ($T \sim 10^{5-6}$ K) component, using O VI $\lambda\lambda 1032, 1038$ [Heckman et al. 2001 (NGC 1705)]. The existence of outflows can be inferred from the presence of absorption lines that are blueshifted with respect to the systemic velocity of the host galaxy. We apply this technique to the warm neutral gas in a sample of 12 ULIGs using the Na I D doublet and measure individual outflow properties such as absorbing column density and outflow velocity. Heckman et al. (2000) (hereafter HLSA) have used this feature to study a sample of 27 luminous infrared galaxies (LIGs; $L_{\text{IR}} > 10^{11} L_{\odot}$) and 5 ULIGs with $z < 0.12$, but generally at lower resolution (55 – 170 km s $^{-1}$). We analyze the line profiles in our targets by means of a χ^2 minimization fitting algorithm that allows for non-Gaussian intensity profiles, multiple absorbing components, and a covering fraction that is less than one. Assuming that all absorption components with velocities greater than ~ 70 km s $^{-1}$ are outflowing, we use a simple model of a mass-conserving free wind to compute the corresponding mass outflow rates. We also compute star formation rates from infrared luminosities.

The ratio of the total mass outflow rate to the corresponding global star formation rate in each object is a measure of the “reheating efficiency,” or the efficiency with which star

bands given in Perault (1987) (see also Sanders & Mirabel 1996), $H_0 = 75$ km s $^{-1}$ Mpc $^{-1}$, and $q_0 = 0$.

formation reheats the surrounding ISM and produces bubbles and outflows (Martin 1999). Previous measurements of the reheating efficiencies in nearby dwarf galaxies, edge-on spirals, and lower-luminosity infrared galaxies indicates that this ratio is of order unity (Martin 1999; HLSA). We can also track the dependence of the reheating efficiency on the mass of the galaxy, as parameterized by observed R - and K' -band luminosities and the kinematics of the host galaxy. We can estimate the fraction of absorbing gas that escapes the galaxy and enters the intergalactic medium by comparing outflow velocities with escape velocities based on measured kinematics. From the reheating efficiency and escape fraction for each object, we are able to compute the “ejection efficiency,” which is the ratio of the outflow rate of material that escapes into the intergalactic medium to the corresponding global star formation rate. This last quantity is most directly related to the impact of ULIGs on the IGM.

The structure of this paper is as follows. Section 2 describes the sample, observations, and data reduction. In §3, we present an analysis of the Na I D lines; measure kinematics, optical depths, and covering fractions; and compute absorbing column densities. We also present equivalent width measurements of prominent absorption lines. In §4, we discuss and interpret the results; we compute mass outflow and star formation rates and compare the results to previous studies; and we discuss the ultimate fate of the outflowing gas. In §5, we summarize and conclude. For all calculations, we assume $H_0 = 75 \text{ km s}^{-1} \text{ Mpc}^{-1}$ and $q_0 = 0$. All wavelengths are vacuum wavelengths unless otherwise noted and are taken from Morton (1991) and/or the NIST Atomic Spectra Database⁶.

2. SAMPLE, OBSERVATIONS, AND DATA REDUCTION

Our targets come from the IRAS 1 Jy survey (Kim & Sanders 1998). The results of this survey are a complete sample, down to a flux level of $f_\nu(60 \mu\text{m}) = 1 \text{ Jy}$, of 118 ULIGs with Galactic latitude $|b| > 30^\circ$ and declination $\delta > -40^\circ$. These objects have redshifts of $z = 0.02 - 0.27$ and are the brightest sources with luminosities in the range $\log(L_{\text{IR}}/L_\odot) = 12.00 - 12.84$. Using low-dispersion optical spectra of resolution 8.3 \AA (Kim et al. 1998; Veilleux, Kim, & Sanders 1999a), we visually selected 11 objects with most or all of the following characteristics: (1) Na I D absorption is deep and possibly blueshifted from systemic; (2) He I $\lambda 5876$ emission is weak or absent; and (3) the Na I D lines are unaffected by the O₂ A- and B-bands near 7620 \AA and 6880 \AA , respectively. The first selection criterion is not necessarily a robust one, since covering fractions less than one are

⁶The NIST Atomic Spectra Database is available at <http://physics.nist.gov/cgi-bin/AtData/main.asd>.

typical in the sample (§3.4) and it is sometimes difficult to determine velocity shifts from systemic using the low-dispersion spectra. Various other selection criteria were operative, as well. For instance, the bulk of our observing window included only 30% of the entire sample, and F04313 – 1649 was chosen solely for its comparatively high redshift. We also tried to choose objects whose energy output is dominated by star formation, rather than an AGN (i.e. H II-region-like objects and LINERs; Lutz et al. 1999). We note that the first selection criterion may create a bias in the sample towards objects with high optical depths and velocities relative to systemic; this possibility should be noted when considering the results. However, the limited window of visibility during the observations and the other selection criteria involved means that this is probably not a strong bias.

Table 1 lists the objects we selected and some of their relevant properties. The optical spectral types are distributed as follows: 2 H II-region-like objects; 7 LINERs; and 3 Seyfert 2s. The object F10190 + 1322 has two nuclei that are well-separated by 6.2 kpc; we classify each nucleus separately based on our data, although the overall spectral class is H II-region-like (Veilleux et al. 1999a). Based on R - and K' -band images (Veilleux et al. 2002), all of the other targets are mononuclear. The same images reveal that some objects have tidal tails, and that all targets show some sign of a recent merger, such as morphological asymmetry.

Table 1 lists a twelfth object, F12540 + 5708 (or Mrk 231). Mrk 231 is an optically classified Seyfert 1, and it contains high-velocity, broad, and deep absorption lines that are reminiscent of broad absorption line quasar spectra. Because of its distinct quasar-like properties, we treat Mrk 231 separately from the rest of the sample, and discuss it only in Appendix A.

We observed the targets at the W.M. Keck Observatory on Keck II using the Echellette Spectrograph and Imager (ESI). In the echellette configuration, ESI is a high-efficiency, moderately-high resolution spectrograph that operates in low, cross-dispersed orders. It has a constant $11.4 \text{ km s}^{-1} \text{ pixel}^{-1}$ dispersion; a wavelength coverage of $0.39 - 1.10 \mu\text{m}$; and a pixel scale of $0''.128 - 0''.179 \text{ pixel}^{-1}$ along the slit (increasing from blue to red orders). ESI operates with a MIT-LL 2048×4096 CCD. We chose a slit width of $1''.0$ and a north-south position angle ($\text{PA} = 0^\circ$) for all observations. From fits to sky lines in the seven reddest orders in our data, we estimate a constant spectral resolution of $R \sim 4600$ for our observations, which corresponds to 65 km s^{-1} . Table 1 lists the UT date of observation and the exposure time for each object, as well as the mean seeing for each night. All observations were made in photometric conditions. The resulting signal-to-noise ratio of the data for most targets is $20 - 40$ per pixel (at maximum sensitivity), although for the brightest targets it is much higher.

We performed the initial data processing using the MAKEE⁷ data reduction package, written by T. Barlow for use with HIRES spectra and adapted to reduce ESI data. MAKEE performs the following automatically: bias subtraction, flat-fielding, order-tracing, sky subtraction, object extraction, and wavelength calibration (including a heliocentric velocity correction and an air-to-vacuum wavelength conversion). MAKEE also produces error spectra based on Poisson statistics, which we propagated consistently through the rest of the reduction procedure and used as input for the minimization algorithms in our spectral fitting routine (§3.1). In most cases, CuAr, HgNe, and Xe lamps were used simultaneously for wavelength calibration; sky lines were later used to apply a constant shift to the solution (the resulting residuals are generally ± 0.2 pixel). The entire spatial profile was extracted for each object; this is the most practical treatment due to the difficulty of maintaining a constant spatial aperture over the large range of z in our sample, the fact that most of the objects are distant and not well-resolved, and the need to maximize the signal-to-noise ratio of the spectra. Flux calibration was done in IRAF using the stars HD 37129 and HD 118246 and corresponding flux points spaced at intervals of 0.7 \AA (Goodrich & Veilleux 1988), avoiding those portions of the stellar spectra with deep absorption lines. A 200 \AA slice of the continuum around each Na I D feature (450 \AA in the case of Mrk 231) was fit with a low-order spline, and the result was divided into the original spectrum to produce a spectrum normalized to unity at the continuum level. (We used a similar normalization procedure for other absorption lines that were fit; see §3.5 and Appendix A.)

3. RESULTS

This section and the following one present the analysis and discussion of our observations. We do not include Mrk 231 in this discussion, except for a brief treatment of its redshift in §3.2 and Table 4 and a mention of its velocity dispersion in Table 7. We discuss Mrk 231 separately in Appendix A. We also treat the two nuclei of F10190 + 1322 separately when appropriate.

3.1. Line Fitting

In the case where the members of a doublet are decently resolved and unblended with each other or other lines, it is possible to compute column density and covering fraction for the absorbing species as a function of velocity (e.g. Barlow & Sargent 1997; Hamann et al.

⁷MAKEE is available at <http://www2.keck.hawaii.edu:3636/realpublic/inst/common/makeewww/index.html>.

1997; Arav et al. 1999a,b; see Appendix A for an example using Ca II H & K in Mrk 231). However, due to the small velocity separation of the Na I D lines ($\sim 300 \text{ km s}^{-1}$), the two profiles are generally too blended with each other for this procedure. Instead, we make the curve-of-growth assumption of a Gaussian velocity distribution and fit multiple components to each line profile. This technique is fairly robust; even if the overall profile is a sum of many Gaussian profiles, the fit of the overall profile will yield roughly accurate column densities and a representative velocity spread (assuming that there are no kinematically narrow but optically thick lines, or unresolved saturated structures; Jenkins 1986; Savage & Sembach 1991). We account for the possibility of covering fractions that are less than one by assuming a covering fraction for each fitted component that is independent of velocity.

Figure 1 displays a $\sim 80 \text{ \AA}$ portion of the spectrum around the Na I D line for our eleven program galaxies, smoothed using a boxcar average of width 3 pixels (corresponding to 34 km s^{-1}). Overlaid on these spectra are our fits to the line profiles. Dashed lines indicate the individual components of each fit. The profiles were fit using a χ^2 minimization routine within the IRAF-based interactive spectral fitting software SPECFIT⁸ (Kris 1994). We added an extra routine to SPECFIT in order to fit absorption doublets with a partial covering fraction. Each fit consisted of several components: a flat continuum; one or more Na I D absorption components (where one component equals one doublet pair); and, when necessary, a He I $\lambda 5876$ emission component. Table 2 lists the parameters that we measured for each absorption component.

The wavelengths in vacuum of the two lines of the Na I D doublet are $\lambda_1 = 5897.558 \text{ \AA}$ and $\lambda_2 = 5891.583 \text{ \AA}$ (Morton 1991), and their oscillator strengths are (to 1% accuracy) in the ratio 2:1, respectively, so that the optical depth at the centroid of the blue line is twice that at the centroid of the red line (i.e. $\tau_{2,c} = 2\tau_{1,c}$). For each doublet component, we fit four parameters: the central optical depth of the weaker, red line, $\tau_{1,c}$; the centroid of the weaker line, λ_1 ; the full width at half-maximum (FWHM) of the physical velocity distribution of the absorbing gas; and a covering fraction, C_f . The central optical depth of the stronger, blue line, $\tau_{2,c}$, then follows from the above relation, and λ_2 follows from the ratio of the two rest wavelengths, which is independent of redshift and relative velocity.

Assuming a continuum level of unity and a covering fraction C_f , the intensity (measured from zero) across the doublet as a function of wavelength is

$$I(\lambda) = 1 - C_f(1 - \exp\{-[\tau_1(\lambda) + \tau_2(\lambda)]\}), \quad (1)$$

where $\tau_1(\lambda)$ and $\tau_2(\lambda)$ are the optical depths in the weak and strong lines, respectively, as

⁸SPECFIT is available at www.pha.jhu.edu/~gak/specfit.html.

a function of wavelength. The curve-of-growth assumption of a Gaussian in velocity space leads to a Gaussian in optical depth for each doublet line. Substituting this optical depth profile into the above equation and using the relationship between $\tau_{1,c}$ and $\tau_{2,c}$ leads to

$$I(\lambda) = 1 - C_f(1 - \exp\{-\tau_{1,c}[e^{-(\lambda-\lambda_1)^2/(\lambda_1 b/c)^2} + 2e^{-(\lambda-\lambda_2)^2/(\lambda_2 b/c)^2}]\}), \quad (2)$$

where b is the Doppler parameter in km s^{-1} [$b = \sqrt{2}\sigma = \text{FWHM}/(2\sqrt{\ln 2})$] and c is the speed of light. This equation applies in both the rest frame and the observer’s frame.

Note again that we make the assumption that the covering fraction C_f is independent of velocity, and hence λ , for a given component. C_f is also technically an “effective” covering fraction in the sense that it describes the fractional area of the background light source that is obscured by the absorbing gas *as well as* any continuum light that may be scattered into the line of sight. Two or more absorbing components within a given object may have different covering fractions; for simplicity in the fitting, we assumed that for n components, each having intensity I_i as given by equation (2), the total intensity reaching the observer is $I_{\text{tot}} = \prod_{i=1}^n I_i$. Modulo the scattered light, this means physically that C_f for a given component describes not only the covering fraction of the background light, but also the fraction of other components that it overlaps with (although the material can be either behind or in front of these other components). The gas can be distributed arbitrarily along the line of sight.

The He I $\lambda 5876$ emission line was fit with a Gaussian intensity profile. In five objects there was no obvious emission, so no line was fit. This component has two free parameters: the FWHM of the Gaussian and the integrated flux under the line. In all cases, we constrained the line center to be at or near the systemic velocity of the galaxy. Again, for simplicity in the fitting, we assumed that $I_{\text{tot}} = I_{\text{emission}} \times I_{\text{absorption}}$, where I_{emission} and $I_{\text{absorption}}$ are both measured from zero; this means that C_f also describes the fractional coverage of the line-emitting region.

There may be another important consideration in the line fitting. The Na I D line in the spectra of galaxies is produced by both stellar and interstellar absorption, but we are interested solely in the interstellar component. To estimate the magnitude of the stellar contribution to the line in each object, we measured the equivalent width of the Mg I b $\lambda\lambda 5167, 5173, 5185$ feature (Table 3), which is mostly stellar in origin. Furthermore, Mg and Na are produced in roughly the same nuclear processes in hot stars, suggesting that there may be a correlation in the abundance of these two elements within stellar atmospheres. To determine this correlation, we used equivalent width data from Heckman, Balick, & Crane (1980) on the nuclei of nearby bright galaxies and from Bica & Alloin (1986) on Galactic globular clusters and a sample of mostly non-active galaxies. Using these data sets, we determined that $W_{\text{eq}}^*(\text{Na I D}) \sim 0.5 W_{\text{eq}}^*(\text{Mg I b})$, with a possible intrinsic scatter of

$\gtrsim 25\%$. The resulting estimates of the fractional contribution of stellar absorption to the Na I D lines in these objects are small (see Table 2); they are in the range 4 – 28%, and have a median and mean value of 15% [with a $\sim 2\text{-}3\ \sigma$ error of $\pm 5\%$ due to uncertainty in the measurement of $W_{\text{eq}}^*(\text{Mg I b})$]. Due to the difficulty of modelling high-resolution profiles of stellar absorption lines that are integrated across an entire galaxy and the fact that the stellar contribution is quite small, we chose to fit the Na I D lines without subtracting the stellar absorption or including a stellar component in our fits. The stellar contribution to the line will likely increase the measured optical depths and covering fractions but decrease the measured blueshift; these effects will, to some degree, offset each other in the estimation of mass outflow rates (eq. [12]).

3.2. Kinematics

The heliocentric redshifts listed in Tables 1 and 4 were determined from the current optical dataset using prominent emission and absorption lines, except in the cases of F05189–2524 and Mrk 231, for which we used the more precise redshifts determined from CO emission (Sanders, Scoville, & Soifer 1991) and H I absorption (Carilli, Wrobel, & Ulvestad 1998), respectively. We measured separate redshifts for stellar absorption lines and nebular emission lines and averaged the two if they differed by no more than $\Delta z = \pm 0.0002$; otherwise, we adopted the absorption-line redshift. Possible errors include: the $65\ \text{km s}^{-1}$ resolution of our spectra; the lower signal-to-noise ratio in those parts of the spectrum where the absorption lines fall; and systematic uncertainties due to unusual kinematics in a few cases. After accounting for these errors, the optical redshifts have a $\sim 2\text{-}3\ \sigma$ uncertainty of ~ 0.0002 (or $60\ \text{km s}^{-1}$). The vertical dotted lines in Figure 1 indicate the wavelengths of Na I D and He I $\lambda 5876$ at the systemic velocity of each galaxy determined from these redshifts.

In Figure 2, we plot the distributions of five kinematic quantities measured from the Na I D profile fits. The velocity centroids relative to systemic for each component are

$$\Delta v \equiv v_{\text{sys}} - v, \quad (3)$$

where v_{sys} is the heliocentric velocity of the host galaxy and v is the heliocentric velocity of the centroid of the absorbing gas component. (Note that we use the opposite of the usual convention—velocities blueshifted relative to the host galaxy are positive.) A “maximum” blueshifted velocity for each component is given by

$$\Delta V = \Delta v + \frac{1}{2}\text{FWHM}. \quad (4)$$

An interesting subset of these two distributions is the maximum Δv and ΔV for each object,

given by

$$\Delta v_{\max} = \max(\Delta v) \quad (5)$$

$$\text{and } \Delta V_{\max} = \max(\Delta V). \quad (6)$$

(“Maximum” here accounts for sign—in other words, it describes the most blueshifted velocity, or least redshifted velocity if no blueshifted velocity exists.) A final kinematic quantity is the distribution of Doppler parameters b for all components. The measured values for FWHM are corrected in quadrature for the instrumental resolution of 65 km s^{-1} before conversion to b (the same correction is made throughout this paper for FWHM). Values for Δv , ΔV , and b for each component are also listed in Tables 2 and 5. The $\sim 2\text{-}3 \sigma$ uncertainty in these measurements varies from source to source, but is on the order of $40 - 60 \text{ km s}^{-1}$ (due to uncertainties in the measured redshifts, the effects of finite instrumental resolution, and uncertainties in the fitting).

The median and mean values, respectively, of each of these distributions are as follows: (a) Δv , 104 km s^{-1} and 233 km s^{-1} ; (b) ΔV , 268 km s^{-1} and 444 km s^{-1} ; (c) Δv_{\max} , 284 km s^{-1} and 381 km s^{-1} ; (d) ΔV_{\max} , 511 km s^{-1} and 636 km s^{-1} ; and (e) b , 200 km s^{-1} and 254 km s^{-1} . Most components (12 of 19, or 63%) have velocities Δv that are blueshifted more than 70 km s^{-1} from systemic—i.e. $\Delta v > 70 \text{ km s}^{-1}$ —and most objects (8 of 11, or 73%) have a maximum velocity $\Delta v_{\max} > 70 \text{ km s}^{-1}$. This percentage can be compared to other recent results. In their study of 32 local LIGs, HLSA find that 38% of their sample hosts outflows, while Pettini et al. (2001) find evidence for outflows in 100% of their 19-member, $z \sim 3$ sample.

For the purposes of calculating mass outflow rates (§4.1), we assume that most blueshifted components represent outflowing material. There are two blueshifted components within 15 km s^{-1} of systemic; we assume this is quiescent interstellar material. However, the other blueshifted components have velocities in excess of 70 km s^{-1} . Note that stellar contamination of the line will bias toward $\Delta v = 0 \text{ km s}^{-1}$ those near-systemic components that are truly outflowing. Note also that substantial systematic errors in redshift could lead to larger than expected errors in Δv . Another important consideration is the fact that most or all ULIGs are mergers in late stages of interaction (Sanders & Mirabel 1996; Veilleux et al. 2002). The interstellar medium in some of these galaxies may then contain tidal material leftover from earlier stages, which could account for the redshifted material observed in a few objects (material with $\Delta v < -100 \text{ km s}^{-1}$ is observed in two objects). This may also account for a small portion of the blueshifted material that we attribute to outflows. Unfortunately, it is not possible to distinguish these two effects without spatial information.

The Doppler parameter b describes the kinematic spread of the absorbing material. Assuming that the absorber is gas that is entrained in a wind, the rather large values that

we measure for b are likely due to the fact that we are simultaneously detecting material from all parts of the outflow. In other words, unresolved projection effects will produce a large range of radial velocities along our line of sight, and multiple components with smaller values of b may blend together and mimic a single component with a large b (Jenkins 1986). The case of a fragmented superbubble (in the blowout stage of a galactic wind) or a clumpy ISM would be consistent with this. Turbulent motion created by shocks in the outflow will also contribute to the observed velocity widths.

In §4.1 we assume that the outflowing gas motions are purely radial. It is also likely, based on observations of local galactic winds (e.g. Heckman et al. 1990; Veilleux et al. 1994; Shopbell & Bland-Hawthorn 1998; Veilleux & Rupke 2002), that the solid angle into which the wind is outflowing is less than 4π , typically due to a collimated, biconical wind structure. If we then assume a point source for the background continuum, our velocity measurements represent actual outflow velocities. However, if the background source is extended and we are not looking down the axis of the assumed biconical wind structure, then projection effects may cause our measurements to underestimate the actual outflow velocities.

3.3. Optical Depth and Column Density

The central optical depth of the weak line, $\tau_{1,c}$, for each component is listed in Table 2, and the distributions of this quantity for all components and only those components assumed to be outflowing are plotted in Figure 3a. The median and mean of these distributions are 0.42 and 0.83, and 0.39 and 0.97, respectively, and the ~ 2 -3 σ uncertainty in $\tau_{1,c}$ is $\sim 25\%$. The corresponding Na I column densities for each component are listed in Table 5 and plotted in Figure 4. We also show in Figure 4 the column densities for only outflowing components and the total column density for each object, summed over only outflowing components. These column densities are computed from $\tau_{1,c}$ and b using (Spitzer 1978)

$$N(\text{Na I}) = \frac{\tau_{1,c} b}{1.497 \times 10^{-15} \lambda_1 f_1}, \quad (7)$$

where $f_1 = 0.3180$ is the oscillator strength of the weak line (Morton 1991), b is in km s^{-1} , and λ_1 is in \AA (in the rest frame, in vacuum). The median and mean values for $N(\text{Na I})$ are: (a) for each component, $3.0 \times 10^{13} \text{ cm}^{-2}$ and $4.3 \times 10^{13} \text{ cm}^{-2}$; (b) for only components assumed to be outflowing, $3.3 \times 10^{13} \text{ cm}^{-2}$ and $5.0 \times 10^{13} \text{ cm}^{-2}$; and (c) for each object, $3.6 \times 10^{13} \text{ cm}^{-2}$ and $5.5 \times 10^{13} \text{ cm}^{-2}$.

In Table 2, we also list the doublet equivalent width ratio for each absorbing component, $R = W_{\text{eq}}^{\lambda 5890} / W_{\text{eq}}^{\lambda 5896}$. These values are not actually measured, but rather computed using synthetic profiles based on the measured profile parameters.

Note that if the wind is collimated and the axis of the outflow is nearly in the plane of the sky, it is possible that very little of the wind will be in front of a strong background continuum source. This could be true for some of the galaxies in our sample, in which case the real distributions of τ and $N(\text{Na I})$ for outflows in these objects will be higher than we measure.

On average, our measured optical depths are a factor of ~ 4 – 10 less than those measured by HLSA in the Na I D line for their sample of 32 starburst-dominated LIGs and ULIGs. For their subsample in which the Na I D doublet is dominated by interstellar absorption, HLSA find a median value of $\tau_{1,c} \sim 4$ using the doublet ratio method and $C_f = 1$. For three objects with cleanly resolved doublets and $C_f \sim 0.8$, they find $\tau_{1,c} \sim 2$. However, the values that they infer for $N(\text{Na I})$ are in the range $(5 - 10) \times 10^{13} \text{ cm}^{-2}$, which is comparable to our column density distribution.

The details of our fitting algorithm relative to that of HLSA may be the cause of the discrepancies among our values for $\tau_{1,c}$. We use a different program (“specfit” vs. “splot”), fit one to three components, and fit Gaussians in optical depth, rather than intensity. An alternative explanation for the differences in the two datasets is a real physical difference in the two samples, which is a possibility given that ours is composed only of ULIGs, while the HLSA sample consists mainly of lower-luminosity galaxies. It should again be emphasized, however, that the resulting total column densities are similar in each case.

Two methods exist for converting $N(\text{Na I})$ to a hydrogen column density. The first (“method 1”) requires making the proper ionization and depletion corrections separately. For cool gas along the line-of-sight to ζ Oph ($l = 6^\circ 28$, $b = +23^\circ 59$, $d = 140$ pc), Morton (1974, 1975) uses a simple photoionization model with electron density $n_e = 0.7 \text{ cm}^{-2}$ and kinetic temperature $T = 56$ K to compute $N(\text{Na II})/N(\text{Na I}) = 3.1$. The corresponding depletion value, taken in reference to the total neutral atomic plus molecular gas [$N(\text{H I}) + 2N(\text{H}_2)$], is then -0.90 . [Savage & Sembach (1996) use different solar reference abundances and infer a depletion value of -0.95 .] Data from Phillips, Pettini, & Gondhalekar (1984) along sightlines toward nine stars near the Galactic plane indicate that the depletion correction for Na is independent of the line-of-sight gas density, suggesting that this value is fairly robust. However, the ionization correction will be more dependent on local physical conditions, and is almost certainly larger than 3.1 in our objects (especially considering that the temperature is probably at least two orders of magnitude larger than 56 K). In general, the physical conditions in outflowing gas in ULIGs are likely to be harsher than along sightlines through the local Galactic ISM. Specifically, shock ionization due to the fast motion of the wind through the quiescent ambient medium and photoionization due to a background continuum from stars, an AGN, and/or hot wind material are likely to produce a higher ionized fraction

of Na (and H).

A second method (“method 2”) uses an empirically-determined factor to convert directly from $N(\text{Na I})$ to $N(\text{H})$ —also derived using data from sightlines through the local Galactic ISM—thus performing the depletion and ionization corrections at once. The relation is of the form

$$\log[N(\text{Na I})] = \beta \log[N(\text{H})] + \gamma, \quad (8)$$

where $N(\text{H})$ may refer to only neutral atomic gas (H I) or both atomic and molecular gas, and column densities are in units of cm^{-2} . In Table 6, we compare values for β and γ from the literature and the size of the conversion factor relative to method 1 [i.e. the ratio of $N(\text{H})$ determined using each method]. In all cases where both β and γ are available, method 2 produces a larger correction by factors ranging from 5 to 41. The correction factor is not uniform across our dataset, either, except for values of β close or equal to unity. In other words, for values of β not equal to unity, the correction factor probably has a dependence on density, n_{H} . (The specific value of β may indicate something about the ionization of the ISM; see Hobbs 1974a, 1976.) For our work, we choose the conversion relation derived by Stokes (1978). It is similar to the earlier results of Hobbs (1974a,b, 1976), and is partly based on this work. The value derived by Ferlet, Vidal-Madjar, & Gry (1985) for β is probably too small, largely due to the subdivision of $N(\text{H})$ along some lines of sight into multiple kinematic components (Herbig 1993). Herbig (1993) includes no values for γ , unfortunately, making his values for β impossible to use.

Our choice of method 2 with $\beta = 2.11$ and $\gamma = -31.3$ means that our values for $N(\text{H})$ are a factor of 6 – 29 higher than those determined from the depletion correction alone [with the actual value dependent on $N(\text{Na I})$], or, if we include an ionization correction of 3.1 in method 1, a factor of 2 – 9 higher. In other words, the effective ionization correction that we make using method 2 is much larger than in method 1. Our values for $N(\text{H})$ are at most a factor of two larger than those of HLSA (although the uncertainty of this conversion applies to their results, as well). However, we still do not know how physical conditions in the gas from which this correction is determined compare to those in the absorbing gas in galactic winds. As discussed above, the conditions in galactic winds are likely to produce a higher level of ionization, suggesting that these estimates for $N(\text{H})$ are still a lower limit to the real values.

3.4. Covering Fraction

The measured covering fraction for each component is listed in Table 2 and the distributions for all components and only those components assumed to be outflowing are plotted

in Figure 3b. The median and mean of these distributions are 0.61 and 0.59, and 0.61 and 0.56, respectively. The measurement error in this quantity is ~ 0.1 .

As discussed in §3.1, the covering fraction gives information about the spatial distribution of the gas, as well as any light that is scattered into the line of sight. Even in the case that it describes solely the amount of absorbing material in front of the continuum source, there are still degenerate configurations which are impossible to distinguish without more spatial information. If the size of the background light source is small compared to the global size of the absorbing gas structure, then the covering fraction is likely to describe the local clumpiness of the absorbing material. However, if the background light is much more extended, then it will also contain information about the global angular size of the absorbing region with respect to the background light.

We state in §3.3 that if the outflow is collimated and its axis lies nearly in the plane of the sky, then the outflow may cover very little of the galactic continuum source. Lower covering fractions could also result from this inclination effect.

3.5. Other Blueshifted Absorption Lines

There are other absorption lines of interest which potentially contain information about the outflows in these objects, such as Ca II H & K and K I $\lambda\lambda 7665, 7699$. The K I doublet typically has a very low signal-to-noise ratio because K I is much less abundant than Na I and the feature is typically redshifted into areas of our spectra where sensitivity is low and night sky lines are prominent. However, the stronger doublet line has a high enough signal-to-noise ratio in six objects to make a measurement of the velocity centroid and gaussian FWHM possible. For ~ 3 of these objects (F03250 + 1606, F09116 + 0334, and F11387 + 4116), both the offsets and widths match those determined for one Na I component to within $\sim 30\%$. However, there are larger discrepancies for the other objects; we attribute these errors to the existence of multiple components and the low signal-to-noise ratio of the K I lines. Because the weak line of the doublet has too low a signal-to-noise ratio to be useful, we are unable to use it as a diagnostic in any object and cannot constrain the K I optical depth or covering fraction.

The Ca II H & K lines are highly contaminated by stellar absorption for low values of Δv . The datasets that we used to infer the relationship between the equivalent widths of Mg I b and Na I D (Heckman et al. 1980; Bica & Alloin 1986) imply that $W_{\text{eq}}^*(\text{Ca II K}) \simeq 2 W_{\text{eq}}^*(\text{Mg I b})$. Based on our measured absorption line equivalent widths (Table 3), we then expect the average stellar contribution to Ca II K to be $\sim 35 - 40\%$; since this

is a substantial fraction of the line, we are unable to treat it as primarily interstellar in origin. However, in one instance, a high-velocity component is well-separated from the near-systemic components, the $\Delta v = 1540 \text{ km s}^{-1}$ line in F05024–1941. Although this part of the spectrum has a lower-than-average S/N, we were able to fit the profiles of these lines (fixing the covering fraction to be the same as for Na I D). The results are as follows: $\tau_{1,c} = 0.6$; $\lambda_1 = 4713.1 \text{ \AA}$; $b = 104 \text{ km s}^{-1}$; $\Delta v = 1559 \text{ km s}^{-1}$; and $N(\text{Ca II}) = 2.9 \times 10^{13} \text{ cm}^{-2}$. Note that the values of Δv determined from Ca II and Na I agree to within the specified errors. However, extrapolating to a hydrogen column density is difficult, largely because of the strong dependence of Ca depletion on density (Phillips et al. 1984), which may contribute to the fact that $N(\text{Ca II})$ and $N(\text{H})$ are not well-correlated along local Galactic sightlines (Hobbs 1974b). The depletion for Ca measured toward ζ Oph is -3.73 (Savage & Sembach 1996), a full factor of 10^3 larger than that measured for Na (-0.95). Using this value yields a larger $N(\text{H})$ than that measured from Na, but it is likely that Ca is actually less depleted than this. For instance, if dust grains are destroyed by the shocks present in these outflows (Phillips et al. 1984; Savage & Sembach 1996), then the Ca depletion and $N(\text{H})$ determined from Ca will both decrease.

3.6. Absorption Line Equivalent Widths

We measured the equivalent widths of the absorption lines used in this paper using “splot” in IRAF; the results are listed in Tables 2 and 3. We quote rest-frame equivalent widths, which are related to the observed equivalent widths by $W_{\text{eq}}^{\text{rest}} = W_{\text{eq}}^{\text{obs}}/(1+z)$. To measure the Na I D equivalent widths, we used the same continuum-normalized sections as in the line fitting. We used the command in “splot” that directly measures W_{eq} given two endpoints, selecting the boundaries by eye (and stopping where the line rose to the continuum level or the He I emission line). For the other lines, the measurements were generally made using a Gaussian fit in “splot,” with no prior continuum fitting. We made no corrections due to broadening of the lines by the intrinsic velocity dispersions of the objects (see Terlevich, Díaz, & Terlevich 1990). The Na I equivalent widths are reasonably accurate ($\pm 5\%$), while those for other lines have a higher uncertainty, roughly $\pm 20\%$ due to uncertainties in continuum placement, lack of sensitivity in the blue and red portions of the spectrum where the lines were typically found, and the presence of sky lines (in the case of the Ca II absorption triplet, $\lambda\lambda 8498, 8542, 8662$). The strengths of the observed lines (the Ca II triplet, Ca II K, the Balmer lines, and Mg I b) suggest that they are produced by a young stellar population with red supergiants superimposed on an older population (Terlevich et al. 1990; Bica, Alloin, & Schmidt 1990).

4. DISCUSSION

4.1. Mass Outflow Rate

The primary purpose of this paper is to estimate total mass outflow rates from the ULIGs in our sample and compare them to the corresponding global star formation rates. We compute mass outflow rates from our measurements and a simple model. Consider a mass-conserving free wind (i.e. the mass outflow rate \dot{M} and velocity v are independent of radius r) in a medium of number density $n(r)$. Assume that the wind flows from an inner radius r_* to infinity, where r_* may correspond to the size of the wind-producing region. The mass outflow rate at a radius r is given by

$$\dot{M} = \Omega C_\Omega r^2 n(r) v m, \quad (9)$$

where Ω is the solid angle subtended by the wind, C_Ω is the angular covering fraction of the gas within the solid angle Ω , and m is the mean particle mass. The total observed column density in the outflow is the integral of n along our line-of-sight:

$$N = \int_{r_*}^{\infty} n(l) dl. \quad (10)$$

Solving equation (9) for $n(r)$, substituting this into equation (10), and integrating leaves us with

$$\dot{M} = \Omega C_\Omega r_* N v m. \quad (11)$$

Normalizing to values typical to our sample and using $m = m_p$ and $C_\Omega = C_f$, we have

$$\dot{M}(\text{H}) = 21 \left(\frac{\Omega}{4\pi} \right) C_f \left(\frac{r_*}{1 \text{ kpc}} \right) \left(\frac{N(\text{H})}{10^{21} \text{ cm}^{-2}} \right) \left(\frac{\Delta v}{200 \text{ km s}^{-1}} \right) M_\odot \text{ yr}^{-1}. \quad (12)$$

Mirabel & Sanders (1989) find that the ratio of molecular to atomic gas in luminous and ultraluminous infrared galaxies increases with increasing far-infrared excess (the ratio of infrared to blue flux), and that ULIGs are likely to have more molecular than atomic gas by a factor of at least 1 – 10. It is unclear how much molecular gas is entrained in galactic outflows, however, so we choose $m = m_p$ as a conservative estimate, rather than $m = 2m_p$. Note also that C_f is distinct from C_Ω in that C_f describes the line-of-sight (rather than angular) covering fraction, and may include information about Ω . However, we use it as a reasonable estimate for, and probably a lower limit to, C_Ω , especially given the probability of inclination effects in our sample.

We compute \dot{M} for each absorbing component with $\Delta v > 70 \text{ km s}^{-1}$ using $\Omega = 4\pi$ and $r_* = 1 \text{ kpc}$ and list the results in Table 5; we assign $\dot{M} = 0 M_\odot \text{ yr}^{-1}$ to all other components.

We also list in this table the total mass outflow rate for each object, \dot{M}_{tot} . The distribution of \dot{M} for each component is plotted in Figure 5a, with a median and mean of $13 M_{\odot} \text{ yr}^{-1}$ and $24 M_{\odot} \text{ yr}^{-1}$; the distribution of \dot{M}_{tot} is shown in Figure 5b, with a median and mean of $22 M_{\odot} \text{ yr}^{-1}$ and $41 M_{\odot} \text{ yr}^{-1}$.

The dominant source of error in \dot{M} , besides our choice of model and any unresolved spatial details, is probably the uncertain conversion of $N(\text{Na I})$ to $N(\text{H})$ (§3.3). However, as discussed above, we likely underestimate the actual values of $N(\text{H})$ and m , suggesting that \dot{M} may be a lower limit. Other sources of error include our inability to measure r_{\star} and Ω . Note that $\Omega < 4\pi$ for many local examples of galactic winds; a change in this quantity will reduce our estimate of \dot{M} by at most a factor of a few. However, we may also underestimate C_{Ω} by using $C_{\Omega} = C_f$, and C_f may include a contribution from Ω due to inclination effects (see above and §3.4). This will mitigate any errors due to our use of $\Omega = 4\pi$. Furthermore, $N(\text{Na I})$ could also be an underestimate due to these inclination effects (§3.3).

4.2. Star Formation Rate and Reheating Efficiency

Table 5 also lists the star formation rate calculated for each of the galaxies in our sample. The star formation rate is proportional to L_{IR} according to (Kennicutt 1998)

$$\text{SFR} = \alpha \frac{L_{\text{IR}}}{5.8 \times 10^9 L_{\odot}}. \quad (13)$$

This equation is based on the stellar synthesis models of Leitherer & Heckman (1995) and assumes the following: a continuous burst of star formation of length 10 – 100 Myr (the mean bolometric luminosity over this age range is used); solar abundances; a Salpeter IMF with mass cutoffs of 0.1 and $100 M_{\odot}$; and that the dust reradiates the bolometric luminosity of the starburst in the infrared (i.e. $L_{\text{IR}} \simeq L_{\text{bolometric}}$). We have included a correction factor α that accounts for the fraction of the bolometric luminosity of the galaxy that is produced by star formation (i.e. $0 \leq \alpha \leq 1$).

Mid- and far-infrared ISO spectroscopy appears to indicate that, on average, the bolometric luminosity of ULIGs is dominated by star formation, rather than an AGN (Genzel et al. 1998). A two-dimensional diagnostic diagram composed of the strength of the $7.7 \mu\text{m}$ PAH feature and mid-infrared line ratios suggests that 70 – 95% of the luminosity of a typical ULIG results from star formation, while the rest comes from an AGN (Genzel et al. 1998). This diagram can be used to roughly estimate the fraction of star formation and AGN activity that contribute to L_{IR} . However, the exact numbers are quite uncertain, and thus should be applied with care. Since ISO spectroscopy exists for only one of the objects in

our sample (F05189 – 2524), we use the available optical spectroscopic classifications (Table 1), which indicate H II-region-like or LINER classifications for most of our objects, to infer that $\alpha \sim 0.8$ is generally applicable to our sample. [Spectral classifications based on optical emission-line ratios and the mid-infrared diagram (or simply the $7.7 \mu\text{m}$ strength) match remarkably well, and comparison of the two suggests that LINERs are starburst-dominated objects (Lutz et al. 1999).] In objects that are optically classified as Seyfert 1s or 2s, the downward correction may be larger, perhaps $\alpha \sim 0.2 - 0.6$. For F05189 – 2524, we choose $\alpha = 0.4$, and for the other two Seyfert 2s, $\alpha = 0.6$. We apply $\alpha = 0.4$ to F05189 – 2524 (an optical Seyfert 2) because it has an obscured broad-line region and has been shown to host a dominant AGN (Veilleux et al. 1999b). Furthermore, Laureijs et al. (2000) give the strength of its $7.7 \mu\text{m}$ feature as 0.4, which is identical to that measured by Genzel et al. (1998) for Mrk 231, an optically-classified Seyfert 1.

The total mass outflow rate in each object normalized to the corresponding global star formation rate,

$$\eta \equiv \frac{\dot{M}_{\text{tot}}}{\text{SFR}}, \quad (14)$$

is labeled the “reheating efficiency” by Martin (1999). We list η for each object in Table 5. For the 8 galaxies hosting a wind, η is in the range $0.07 - 0.66$, with a median and mean of 0.24 and 0.30. For all 11 objects, the median and mean of η are 0.14 and 0.22. These values are lower on average by a factor of ~ 10 than those measured by Martin (1999) for warm ionized and hot X-ray-emitting gas in a sample of ten dwarf and six edge-on spiral galaxies, which have $\eta \sim 0.7 - 5$. HLSA find that the reheating efficiencies for their sample are of order unity, although they do not measure specific values of \dot{M} for each object.

The global star formation rates in the dwarfs and edge-on spirals surveyed by Martin (1999) are much smaller than those in ULIGs, however. The average star formation rate for the dwarf galaxies in the Martin (1999) sample is $\sim 0.08 M_{\odot} \text{ yr}^{-1}$, based on integrated H α fluxes (Martin 1998); this is 3–4 orders of magnitude smaller than the typical star formation rate in ULIGs. The six edge-on galaxies also have lower star formation rates by about two orders of magnitude, based on infrared luminosities from Rand (1996) (although they have areal star formation rates that are comparable to those of dwarf galaxies, when averaged over the entire galaxy; Martin 1999). The galaxies in HLSA that contain outflows (including three ULIGs) have a median infrared luminosity of $L_{\text{IR}} = 2 \times 10^{11} L_{\odot}$, which corresponds to a global SFR of $34 M_{\odot} \text{ yr}^{-1}$, an order of magnitude smaller than in our sample. Finally, the global averaged surface brightnesses in ULIGs (over sizes of a few hundred parsecs, derived from mid-infrared observations) are typically much larger, by factors ~ 100 , than those measured for typical starburst galaxies, including those mentioned above (Soifer et al. 2000; Meurer et al. 1997).

The dense concentrations of molecular gas in ULIGs are likely to provide a large amount of dynamical resistance to any outflow that must travel through them. ULIGs typically contain large amounts of molecular gas in their nuclei, on the order of $10^{10} M_{\odot}$, on scales of less than 1 kpc (e.g. Downes & Solomon 1998). The gravitational potential of these dense nuclei may restrict the outflow, as well.

In light of these considerations, it is remarkable that the reheating efficiencies in these ULIGs are only a factor of 10 lower than those in less massive galaxies. At face value, our results imply that the outflow rate of a galactic wind scales (to within an order of magnitude) with the star formation rate of its host galaxy over a wide range of SFR. Some of the difference in the average η between our study and that of Martin (1999) may be consistent with our suggestion that our values of \dot{M}_{tot} are really lower limits to the actual values. However, it is also possible that the difference in η between the two samples results from the different physical conditions in ULIGs. Finally, we should note that the interstellar gas phases traced by the study of Martin (1999) are hotter and more ionized than the “cool” ($T \sim 10^{3-4} K$) neutral gas to which our survey is sensitive. Thus, the discrepancy may also arise from having more outflowing gas in hotter, ionized gas phases. The relative amount of material in the different interstellar gas phases of an outflow is still uncertain even in nearby objects; future multi-phase studies should shed light on this question.

4.3. Host Galaxy Kinematics, Escape Fraction, and Ejection Efficiency

The fraction of outflowing gas that escapes into the intergalactic or intracluster medium is an important parameter in outflow models for the mass-metallicity relation, the enrichment of the IGM, and galaxy formation. This escape fraction could be measured by comparing estimates of the escape velocity for each galaxy to the outflow velocity of each component.

4.3.1. Host galaxy kinematics

We parameterize the mass and kinematics of each galaxy using five methods: (1) absolute R - and K' -band magnitudes (Veilleux et al. 2002; see Table 1), which trace the stellar populations of each galaxy; (2) the central line-of-sight velocity dispersion, determined from the fundamental plane of ellipticals and often used to represent random stellar motions; (3) the average emission line FWHM and the average FWHM of the Ca II triplet ($\lambda\lambda 8498, 8542, 8662$), probing gaseous and stellar kinematics, respectively, and representing a superposition of random and bulk circular motions; (4) position-velocity diagrams that in-

dicating rotation of the emission-line gas, which are available in a few cases from our spectra; and (5) rotation curves from integral-field spectroscopy of the Pa α line that exist for the two nuclei in F10190 + 1322 (Murphy et al. 2001). See Table 7 for a summary of host galaxy kinematics.

In method 1, the R - and K' -band magnitudes (Veilleux et al. 2002) may trace the mass in older stellar populations. However, we have not corrected the latter for the contribution from supergiants, which for ULIGs could be substantial because of their intense nuclear star formation, or for the low-wavelength tail of far-infrared dust emission, which is sometimes non-negligible at these wavelengths.

ULIGs may be disky ellipticals-in-forma-tion, and those classified as ellipticals based on their surface brightness profiles appear to lie on the fundamental plane (Genzel et al. 2001; Veilleux et al. 2002). In method 2, we use values of the effective radii, r_e , and surface brightnesses, μ_e , measured in the R band (Veilleux et al. 2002) to derive the central line-of-sight velocity dispersion σ_0 for each galaxy from the R -band fundamental plane (Jørgensen, Franx, & Kjaergaard 1996; Hudson et al. 1997). The line-of-sight velocity dispersion is often used to represent random stellar motions, although it observationally depends on the aperture used to measure it and could include a rotational component. Due to the intrinsic scatter on the fundamental plane and measurement uncertainties in r_e and μ_e , these velocity dispersions have an uncertainty of $\sim 30\%$.

The emission and absorption lines used in method 3 are the following: in emission, [O III] $\lambda\lambda 4959, 5007$; [O I] $\lambda 6300$; [N II] $\lambda\lambda 6548, 6583$; H α ; and [S II] $\lambda\lambda 6716, 6731$; and in absorption, the Ca II triplet. We also measured the line widths of H γ – H11 (excluding H ϵ , which is mixed with Ca II H) and Ca II K in absorption, although we do not use these in method 3. In most cases, the emission-line component of the lower order Balmer lines (H β – H δ) was too prominent to yield accurate absorption line widths. We list the results in Tables 8 and 9. For most emission lines, we measured the peak and continuum levels of each line and used these numbers to compute the location of the half-maximum points. This technique was necessary because of the asymmetric nature of many of the strong emission lines. This was done without fitting the continuum around the lines, but the surrounding continuum is generally flat. Most absorption lines were fit with a Gaussian using the “splot” tool in IRAF; the level and slope of the continuum were estimated by eye for each line. The values listed in Tables 8 and 9 are corrected in quadrature for an instrumental resolution of 65 km s $^{-1}$. Measurement uncertainties for these line widths are $\sim 5 - 10\%$ for most emission lines at the $\sim 2-3 \sigma$ level and $\sim 20\%$ for most absorption lines (the absorption line uncertainties are higher due to lower sensitivity toward the red and blue parts of the spectrum, uncertainty in continuum levels, and intervening sky lines at long wavelengths).

We do not use the Balmer lines or Ca II K in method 3 because the Balmer line widths are probably dominated by pressure-broadening rather than the stellar velocity dispersion of the galaxy, and the Ca II K line contains a blend of stellar and interstellar absorption. It is possible that the emission line widths are due to non-gravitational or non-circular motions, such as outflows or interactions; this may be especially true in AGNs for the [O III] lines (Veilleux et al. 1995; Kim et al. 1998). It is also likely that different emission lines trace different parts of the galactic potential due to differences in lower levels, ionization potential, and critical density for de-excitation. Taking an average over many emission lines may mitigate these effects; stellar absorption line widths should be largely free of them, however.

The tilt of the H α line in position-velocity space for several objects is suggestive of a rotation curve. For three of these objects, we are able to estimate a lower limit to the amplitude of the rotation curve using the velocity difference between emission peaks (method 4). These measurements are lower limits due to both unknown inclination effects and the fact that the emission peaks may not represent the full amplitude of the rotation curve (but rather only bright nuclear material). Other objects have tilts, as well, but are too spatially unresolved or have no obvious peaks. Some objects also show evidence for faint, spatially-extended, kinematically-disturbed line-emitting material.

The average emission line FWHM correlates well with the FWHM of the Ca II triplet; see Figure 6. Fitting a linear model that passes through 0 km s $^{-1}$, we arrive at

$$\text{FWHM}_{\text{avg}}^{\text{em}} = (1.02 \pm 0.06) \times \text{FWHM}_{\text{avg}}^{\text{CaII}}, \quad (15)$$

with a correlation coefficient of 0.99. This may imply that the gaseous material and stellar populations traced by these lines have similar kinematics. Furthermore, the measured kinematic quantities roughly correlate in the expected way with the measured luminosities based on the Tully-Fischer and Faber-Jackson relations; that is, more luminous (and more massive) objects have larger values of $\text{FWHM}_{\text{avg}}^{\text{em}}$, $\text{FWHM}_{\text{avg}}^{\text{CaII}}$, and σ . The best correlation is seen in comparing $M_{K'}$ and $\text{FWHM}_{\text{avg}}^{\text{em}}$; see Figure 7.

4.3.2. *Reheating efficiency as a function of galaxy mass*

In order to quantify the dependence of the reheating efficiency on the mass of the host galaxy, we plot it as a function of the measured kinematic quantities and absolute magnitudes in Figure 8. These plots show no clear indication of a relationship between mass and reheating efficiency, even when we consider only objects that are dominated by star formation (objects that are optically classified as H II-region-like or LINERs). This is consistent with the results

of Martin (1999), who finds no correlation between η and maximum H I rotation speed v_c for her sample of less massive galaxies. However, unresolved inclination effects could produce part of the scatter in the plot of η vs. $\frac{1}{2}\text{FWHM}_{\text{avg}}$, if the latter traces rotation.

4.3.3. Escape fraction and ejection efficiency

A related question is how much of the outflow has enough kinetic energy to escape the gravitational potential of its host. To estimate the escape velocity for each galaxy, we assume a singular isothermal sphere potential. For a singular isothermal sphere truncated at r_{max} , the escape velocity v_{esc} at radius r is related to the rotation speed v_c and r_{max} by

$$v_{\text{esc}}(r) = \sqrt{2}v_c[1 + \ln(r_{\text{max}}/r)]^{1/2}. \quad (16)$$

We make a conservative estimate of v_c by choosing the largest of $\frac{1}{2}\text{FWHM}_{\text{avg}}^{\text{em}}$, $\frac{1}{2}\text{FWHM}_{\text{avg}}^{\text{CaII}}$, $\sqrt{2}\sigma_0$, the rotation speed measured in position-velocity space, and, in the case of F10190 + 1322, the measured rotation speeds. This makes the assumption that the FWHMs are largely due to bulk rotational (rather than random) motions, and that σ_0 represents random motions (the factor of $\sqrt{2}$ comes from equating the kinetic energy in bulk rotational and random motions). Given that dark matter halos for these objects may extend to ~ 100 kpc, r_{max}/r is likely to be in the range 10 – 100. We choose $r_{\text{max}}/r = 10$; although this means lower values for v_{esc} , it is fairly insensitive to r_{max}/r anyway (increasing r_{max}/r by a factor of 10, from 10 to 100, only changes v_{esc} by 30%). Our results on the escaping mass fraction also do not depend sensitively on the choice of r_{max}/r , as we demonstrate below.

The escaping mass fraction in each object (Table 5) is defined as

$$f_{\text{esc}} \equiv \frac{\dot{M}_{\text{esc}}}{\dot{M}_{\text{tot}}}.$$

To get \dot{M}_{esc} , we compute the fraction of the equivalent width in each component that lies above the value of v_{esc} determined for each host galaxy, and then sum over all components; this is approximately valid for our sample, since all components are optically thin or close to it. In Figure 9, we show how $\Delta v \pm \frac{1}{2}\text{FWHM}$ (representing the velocity centroid and spread of each component) compares with v_c . Those components with part or all of their profiles above the escape velocity for a given v_c and r_{max}/r will have $f_{\text{esc}} > 0$.

We also define a quantity, similar to the reheating efficiency η , that parameterizes the “ejection efficiency” for each object, or the efficiency with which star formation is able to expel gas from the galaxy:

$$\delta \equiv \frac{\dot{M}_{\text{esc}}}{\text{SFR}}.$$

Note that $\delta = \eta f_{\text{esc}}$. We list δ for each object in Table 5. In their study of the mass-metallicity relation of ellipticals, Kauffmann & Charlot (1998) use a prescription in which $\delta \sim v_c^{-2}$. Although our sample contains only five objects with $\delta > 0$, we find no evidence for this dependence of δ on v_c (or the other kinematic quantities we measure).

We find that $f_{\text{esc}} > 0$ (and thus $\delta > 0$) for 6 out of 12 outflowing components and 5 out of 11 objects (disregarding the one component with $f_{\text{esc}} = 0.01$). Rather than averaging together individual values of f_{esc} and δ , better measures of the global escape fraction and ejection efficiency for ULIGs at $z < 0.3$ are

$$\langle f_{\text{esc}} \rangle = \frac{\sum_{i=1}^{11} \dot{M}_{\text{esc}}^i}{\sum_{i=1}^{11} \dot{M}_{\text{tot}}^i} = 0.49 \quad (17)$$

$$\text{and } \langle \delta \rangle = \frac{\sum_{i=1}^{11} \dot{M}_{\text{esc}}^i}{\sum_{i=1}^{11} \text{SFR}^i} = 0.10 \quad (18)$$

where the sums are taken over all objects but Mrk 231.

These two results are relatively insensitive to the choice of r_{max}/r and the fact that we assumed the FWHMs to be due to rotation, rather than random motions. In the case where we assume $r_{\text{max}}/r = 100$, the result is $\langle f_{\text{esc}} \rangle = 0.41$ and $\langle \delta \rangle = 0.09$. In the case where we assume that the FWHMs trace random motions (i.e. $v_c = \sqrt{2} \frac{1}{2} \text{FWHM}$), $\langle f_{\text{esc}} \rangle = 0.40$ and $\langle \delta \rangle = 0.08$. Assuming both results in $\langle f_{\text{esc}} \rangle = 0.33$ and $\langle \delta \rangle = 0.07$. However, as we increase v_{esc} , the number of objects for which f_{esc} is non-negligible (i.e. greater than a few percent) decreases, such that there are only two remaining objects in the extreme case of assuming large r_{max}/r and random FWHMs.

These results suggest that $\sim 40 - 50\%$ of the total outflowing gas in all ULIGs at $z < 0.3$ escapes into the intergalactic medium, and that star formation is relatively efficient at expelling gas from these galaxies, ejecting $\sim 8 - 10\%$ of the mass of interstellar gas that goes into star formation. However, it should be emphasized that these values are fairly uncertain. We do not know how the radius at which we have computed v_{esc} matches the actual radius of the absorbing gas; we do not have the data to model the potential of these galaxies in detail; and small number statistics or selection biases could play a role in our measurements. Note also that unknown inclination effects could affect our calculation of v_c and v_{esc} ; however, as we discuss above, $\langle f_{\text{esc}} \rangle$ is relatively insensitive to our choice of v_{esc} . Finally, and perhaps most importantly, other forces (e.g. hydrodynamic and magnetic) besides the gravitational force are at work to accelerate or slow the wind (Strickland 2002). For instance, the wind also might end up transferring energy to dense clouds of gas or a dense halo, lose energy in turbulent vortices, or be contained by magnetic fields, in which case the escape fraction is in reality smaller than we measure.

The escape fraction of hot wind material (to which we are insensitive) may be higher, due to its greater specific energy (measured against the binding energy of the galaxy). Hot gas that is interior to a shell of cool, swept-up ambient material in an expanding superbubble is able to exit the bubble when the shell ruptures and fragments. Simulations of dwarf galaxies with low star formation rates suggest that the percentage of this hot material that escapes the galaxy is greater than the percentage of cooler, entrained gas that escapes; further, galaxies with low masses are the most efficient at ejecting this material (Mac Low & Ferrara 1999). These results are not immediately applicable to our sample, since the mechanical energy injection rates from star formation would have to be scaled upward substantially and Mac Low & Ferrara (1999) do not include the possibility of a surrounding dense halo or complex of tidal debris (which may be present around ULIGs if they are created by galaxy interactions). Silich & Tenorio-Tagle (2001) perform a similar study of dwarf galaxies, including the effects of halos and external pressure from the surrounding IGM, and conclude that halos substantially increase the threshold energy required to eject gas into the IGM. In general, more gas than we detect in this survey may actually escape these galaxies unless the large masses of ULIGs or surrounding gas becomes an important factor.

4.3.4. Cosmological implications

What implications do our measurements have for the fractional contribution of ULIGs to the total amount of gas escaping galaxies and entering the intergalactic medium as a function of z ? It is straightforward to show that this fraction is given by

$$Q(z) = P(z) \frac{1}{P(z) + \langle \delta \rangle^{\text{sfg}}(z) / \langle \delta \rangle^{\text{ULIGs}}(z) [1 - P(z)]}, \quad (19)$$

where $P(z)$ is the fractional contribution of ULIGs to the total star formation rate density of the universe at redshift z and $\langle \delta \rangle^{\text{sfg}}(z)$ is the ejection efficiency for all star-forming galaxies other than ULIGs as a function of z . In Figure 10, we plot Q as a function of $\langle \delta \rangle^{\text{sfg}} / \langle \delta \rangle^{\text{ULIGs}}$ for various values of P .

Locally (i.e. our sample at $z < 0.3$), the fraction of total star formation that occurs in ULIGs is modest ($\sim 5\%$; Adelberger 2001). However, because of the strong increase in the number density of ULIGs with z (up to at least $z \sim 2 - 3$; see references in §1), this fraction may increase strongly, as well. If $P(z)$ continues to increase with z , ULIGs at higher z may contribute a significant fraction of the gas being expelled into the IGM. If we assume that $\langle \delta \rangle^{\text{sfg}} / \langle \delta \rangle^{\text{ULIGs}} \sim 10$ at all z (i.e. equal to the value we measure locally), then $P(z)$ must be greater than 50% to get $Q(z) \gtrsim 10\%$. In other words, ULIGs must produce more than half of all star formation at a given z to be responsible for more than 10% of the mass escaping

galaxies and entering the IGM at that z .

5. CONCLUSIONS

We present the results of a moderately-high resolution spectroscopic study of a sample of 11 ULIGs. These objects are selected from the IRAS 1 Jy sample of Kim & Sanders (1998) as good candidates to contain massive, galaxy-scale outflows. (This possible bias toward objects with high mass outflow rates should be considered when assessing the generality of our results.) The goal of the study is to use prominent absorption lines to measure mass outflow rates in these galaxies. Profiles are fit to the Na I D lines in each object to measure column densities, $N(\text{Na I})$; velocities relative to the host galaxy, $\Delta v = v_{\text{sys}} - v$; line widths; and a covering fraction C_f . Our analysis technique assumes a Gaussian velocity distribution for the absorbing gas and fits intensity profiles using a χ^2 minimization; it is useful for fitting profiles with one or two absorbing components (or more if well-separated in velocity space or otherwise constrained), profiles with a covering fraction less than unity, and even slightly saturated profiles.

We measure absorption-line components blueshifted by $\gtrsim 70 \text{ km s}^{-1}$ in 8 of the 11 targets (73%); this stands in between the recent measurements of HLSA and Pettini et al. (2001), who find outflows in 38% and 100% of their sample, respectively. The absorbing material in our sample have relatively low optical depths (mostly $\tau_{\text{I},c} < 1.0$), and the corresponding covering fractions span a wide range. The typical maximum outflow velocity Δv_{max} and total outflowing Na I column density are $\sim 300 \text{ km s}^{-1}$ and $(4 - 5) \times 10^{13} \text{ cm}^{-2}$, respectively (although one object has $\Delta v_{\text{max}} = 1540 \text{ km s}^{-1}$). We also measure the host galaxy kinematics in several ways and present absolute R - and K' -band magnitudes (Veilleux et al. 2002) in order to trace the masses and gravitational potentials of these galaxies. From these data, we infer the following:

(1) *Mass outflow rate.* Using a simple model of a mass-conserving free wind and assuming that all absorbing components with $\Delta v > 70 \text{ km s}^{-1}$ are outflowing, the corresponding total mass outflow rates for objects hosting a wind are in the range $13 - 133 M_{\odot} \text{ yr}^{-1}$. The simplicity of our model and the difficulty of ionization corrections in the conversion from $N(\text{Na I})$ to $N(\text{H})$ likely dominate the uncertainties in \dot{M} . However, the absorbing gas is probably in harsher conditions than we assume, suggesting that our results are lower limits to the actual values.

(2) *Reheating efficiency.* The reheating efficiencies in our sample, equal to \dot{M}_{tot} divided by the corresponding global star formation rate ($\eta \equiv \dot{M}_{\text{tot}}/\text{SFR}$), are in the range $0.1 - 0.7$

for galaxies hosting a wind. These values are on average a factor of only ~ 10 smaller than those measured by Martin (1999), who studied warm ionized and hot gas in a sample of nearby dwarf galaxies and edge-on spirals and concluded $\eta = 0.7 - 5$, and Heckman et al. (2000) (HLSA), who studied a sample of luminous and ultraluminous infrared galaxies and concluded that $\eta \sim 1$. Given that the galaxies in these studies have star formation rates that are, on average, $10 - 10^4$ times smaller than the SFRs in ULIGs, and that molecular gas in ULIGs may inhibit outflows, it is remarkable that their values for η differ by a factor of only 10. This implies that the outflow rate of a wind scales (to within a factor of 10) with the corresponding star formation rate over a wide range of values of SFR, which in turn suggests that the physical conditions governing outflows may be somewhat similar in both ULIGs and less massive galaxies.

(3) *η and δ vs. host mass.* Within our sample, the reheating efficiency apparently has no dependence on the mass of the host galaxy (as traced by emission- and absorption-line widths, central velocity dispersions, M_R , and $M_{K'}$), a result also obtained by Martin (1999). Although our subsample of objects with ejection efficiency $\delta \equiv \dot{M}_{\text{esc}}/\text{SFR} > 0$ is small (~ 5 objects), we also find no evidence that $\delta \sim v_c^{-2}$, a prescription postulated by Kauffmann & Charlot (1998) in their theoretical study of the mass-metallicity relation of ellipticals.

(4) *Escape fraction and ejection efficiency.* We estimate the fraction of absorbing gas in our galaxies which escapes into the surrounding medium by using host galaxy kinematics and a singular isothermal sphere potential to compute v_{esc} and compare it to the outflowing gas velocities. We find that 5 out of 11 objects have non-zero escape fractions, and the resulting average escape fraction of gas is $\langle f_{\text{esc}} \rangle \equiv \sum \dot{M}_{\text{esc}}^i / \sum \dot{M}_{\text{tot}}^i = 0.4 - 0.5$. The corresponding average “ejection efficiency” is $\langle \delta \rangle \equiv \sum \dot{M}_{\text{esc}}^i / \sum \text{SFR}^i = 0.08 - 0.10$. These values are fairly uncertain, and could be compromised by any sample selection bias or the small size of our sample, but are relatively insensitive to the way in which we calculate v_{esc} .

At a given z , the fraction of gas being expelled into the intergalactic medium that originates in ULIGs is governed by two parameters: (1) the fractional contribution of ULIGs to the total star formation rate density of the universe, and (2) the ratio of the average ejection efficiency of other star-forming galaxies to that of ULIGs, $\langle \delta \rangle^{\text{sfg}} / \langle \delta \rangle^{\text{ULIGs}}$. The fractional contribution of ULIGs to star formation is modest in the local universe, but it may increase strongly with z due to the observed strong increase in the number density of ULIGs with z . For $\langle \delta \rangle^{\text{sfg}} / \langle \delta \rangle^{\text{ULIGs}} = 10$ (consistent with current observations), we find that ULIGs must host at least 50% of all star formation at a given z for the fractional contribution of ULIGs to gas ejected from galaxies into the IGM to be greater than 10%.

The authors thank the referee, Tim Heckman, for a thoughtful and detailed referee re-

port. DSR thanks Ray Weymann and Cole Miller for reading versions of the manuscript and helpful discussions and comments. SV is grateful for partial support of this research by a Cottrell Scholarship awarded by the Research Corporation, NASA/LTSA grant NAG 56547, and NSF/CAREER grant AST-9874973. DSR is also supported by NSF/CAREER grant AST-9874973. This research has made use of the NASA/IPAC Extragalactic Database (NED), which is operated by the Jet Propulsion Laboratory, California Institute of Technology, under contract with the National Aeronautics and Space Administration.

A. MARKARIAN 231

Mrk 231 (listed as F12540 + 5708 in Table 1) is the only optically classified Seyfert 1 galaxy in our sample. This object contains broad, complex absorption line systems in low-ionization species, including Na I D, He II λ 3889, and Ca II H and K (Boksenberg et al. 1977; Rudy, Foltz, & Stocke 1985; Hutchings & Neff 1987; Boroson et al. 1991; Forster, Rich, & McCarthy 1995). Some components of these absorption line systems have proven to be time-variable (Hutchings & Neff 1987; Boroson et al. 1991; Forster et al. 1995). The dramatically different nature of these absorption lines compared to those in the ULIGs discussed above (i.e. broader, blacker, and higher velocity), coupled with the fact that Mrk 231 is a Seyfert 1, suggest that their physical origin is distinct.

In Figure 11, we present our observations of and fits to the absorption lines discussed above. Note that Na I D is also present as a broad emission line near systemic, although this is not visible in Figure 11. Using the analysis of Forster et al. (1995) as a starting point, we fit the Na I D lines in this object using 12 narrow components with relatively small optical depths, despite the initial appearance of strong saturation in the profile. Our results are comparable to those of Forster et al. (1995), although we also allowed for a partial covering fraction in each component. Using the velocity components measured in absorption in Na I, we fit the strong absorption features of He I λ 3889 and Ca II H & K. We also constrained the covering fraction in each component to be the same as for Na I (and in a few cases, the FWHM of the component, as well, to avoid broad lines in the fit). The resulting velocity components and values for C_f , τ , b , and N are listed in Table 10. It is important to note that this solution is not very well constrained or unique, given the number of components used to fit each line, suggesting that the parameter values measured in the blended parts of the lines are fairly uncertain. There is also no *a priori* reason to expect that C_f will be the same for different ions, but we make this assumption to provide better constraints on the fit.

In instances where two or more lines from a given ion differing in the product $f\lambda$ are present, a more physically sound way to perform this analysis is to compute the optical

depth and covering fraction as a function of velocity. Because the Na I D doublet lines are closely spaced, this treatment is not possible; however, it is feasible for the Ca II H & K lines, which have a large spacing and an $f\lambda$ (and optical depth) ratio of 2. In Figure 12, we present these Ca lines as a function of Δv ; we have rebinned the spectra into $\log(\lambda)$ space, binned again by 6 pixels (corresponding to 68 km s⁻¹, the resolution of our spectra), and boxcar smoothed by 3 bins. The covering fraction and optical depth in each velocity bin, shown as $(1 - C_f)$ and $e^{-2\tau_1}$ in Figure 11, are then given by (Hamann et al. 1997)

$$C_f = \begin{cases} \frac{I_1^2 - 2I_1 + 1}{I_2 - 2I_1 + 1} & \text{if } I_1 > I_2 \geq I_1^2 \\ 1 & \text{if } I_2 < I_1^2 \\ 1 - I_1 & \text{if } I_2 \geq I_1 \end{cases} \quad (\text{A1})$$

$$\tau_1 = \ln\left(\frac{C_f}{I_1 + C_f - 1}\right) \quad (\text{A2})$$

$$\text{and } \tau_2 = 2\tau_1, \quad (\text{A3})$$

where I_1 (τ_1) and I_2 (τ_2) are the residual intensities (optical depths) in Ca II H λ 3968 and Ca II K λ 3934, respectively. It appears that the covering fraction in this ionization state of Ca is smaller at higher optical depths (i.e. near line center), and that the intensity at higher optical depths is determined by C_f , rather than τ . This result is similar to that found by Arav et al. (1999b) for the Si IV λ 1394, 1403 doublet in the BAL QSO 1603 + 3002, where the line profile becomes optically thick but not black and the residual intensity in the lines is determined by C_f . It also appears that our multi-component fits to Ca II reproduce τ_2 and C_f computed using the above equations in some cases, but not all (see the points in Figure 12). This may also be the case in the He I and Na I lines in our observations, but it is impossible to distinguish the effects of τ and C_f as a function of velocity without more information (i.e. other transitions).

The detailed modelling and interpretation of these results is outside the scope of this paper. However, we do compute a mass outflow rate for Mrk 231 based on our Na I fits. We measure a total outflowing column density of $N(\text{Na I}) = 3.1 \times 10^{14} \text{ cm}^{-2}$, which is slightly higher than the $1.9 \times 10^{14} \text{ cm}^{-2}$ measured by Forster et al. (1995). Normalizing to $r_\star = 1 \text{ pc}$, we get

$$\dot{M} = 5.2 \left(\frac{r_\star}{1 \text{ pc}}\right) M_\odot \text{ yr}^{-1}. \quad (\text{A4})$$

We use a smaller value for r_\star because the energy injection region for the outflow is likely to be smaller, especially given the variability observed in the source and the high velocities, which seem to indicate that the AGN is driving the outflow, rather than the starburst. We do not compute a reheating efficiency for Mrk 231; if the AGN powers the wind, η is probably not a meaningful quantity (since it involves the star formation rate of the host).

The absorption system at $\Delta v = 8060 \text{ km s}^{-1}$ is time-variable. Previous non-detections and detections include the following: (1) 1984 December, Hamilton & Keel (1987), no detection in Na I; (2) 1988 May, Boroson et al. (1991), detection in Na I ($\Delta v = 7760 \text{ km s}^{-1}$ —after conversion to $z = 0.04217$ —and $W_{\text{eq}}^{\text{rest}} = 2.1 \text{ \AA}$) and in He I $\lambda 3889$; (3) 1991 April, Forster et al. (1995), detection in Na I D (7830 km s^{-1} , 1.7 \AA); (4) 1994 April, Forster et al. (1995), detection in Na I D (7860 km s^{-1} , 0.9 \AA). We measure a (rest-frame) equivalent width of 0.36 \AA for this feature at $\lambda_1 = 5983.1 \text{ \AA}$, but we do not detect it in He I or Ca II. (The sensitivity of the spectrograph is declining sharply at the expected location of the He I feature, so the fact that we do not detect it could be due to lack of sensitivity rather than to the absence of the feature.) It is interesting to note that the strength and blueshifted velocity of this feature in Na I D have decreased and increased, respectively, over time.

REFERENCES

- Adelberger, K. L. 2001, in Proceedings of Ringberg Workshop, Starburst Galaxies: Near and Far, ed. D. Lutz & L. Tacconi (New York: Springer)
- Aguirre, A., Lernquist, L., Schaye, J., Weinberg, D. H., Katz, N., & Gardner, J. 2001, *ApJ*, 560, 599
- Arav, N., Korista, K. T., de Kool, M., Junkkarinen, V. T., & Begelman, M. C. 1999a, *ApJ*, 516, 27
- Arav, N., Becker, R. H., Laurent-Muehleisen, S. A., Gregg, M. D., White, R. L., Brotherton, M. S., & de Kool, M. 1999b, *ApJ*, 524, 566
- Barger, A. J., Cowie, L. L., & Sanders, D. B. 1999, *ApJ*, 518, L5
- Barlow, T. A., & Sargent, W. L. W. 1997, *AJ*, 113, 136
- Bica, E., & Alloin, D. 1986, *A&A*, 166, 83
- Bica, E., Alloin, D., & Schmidt, A. 1990, *MNRAS*, 242, 241
- Blain, A. W., Kneib, J.-P., Ivison, R. J., & Smail, I. 1999, *ApJ*, 512, L87
- Boksenberg, A., Carswell, R. F., Allen, D. A., Fosbury, R. A. E., Penston, M. V., & Sargent, W. L. W. 1977, *MNRAS*, 178, 451
- Bond, N. A., Churchill, C. W., Charlton, J. C., & Vogt, S. S. 2001, *ApJ*, 562, 641
- Boroson, T. A., Meyers, K. A., Morris, S. L., & Persson, S. E. 1991, *ApJ*, 370, L19

- Carilli, C. L., Wrobel, J. M., & Ulvestad, J. S. 1998, *AJ*, 115, 928
- Chen, H.-W., Lanzetta, K. M., Webb, J. K., & Barcons, X. 2001, *ApJ*, 559, 654
- Cowie, L. L., & Songaila, A. 1998, *Nature*, 394, 44
- David, L. P., Forman, W., & Jones, C. 1991, *ApJ*, 380, 39
- Dekel, A., & Silk, J. 1986, *ApJ*, 303, 39
- Dove, J. B., Shull, J. M., & Ferrara, A. 1999, *ApJ*, 531, 846
- Downes, D., & Solomon, P.M. 1998, *ApJ*, 507, 615
- Eales, S., Lilly, S., Gear, W., Dunne, L., Bond, J. R., Hammer, F., Le Fèvre, O., & Crampton, D. 1999, *ApJ*, 515, 518
- Efstathiou, A., et al. 2000, *MNRAS*, 319, 1169
- Efstathiou, G. 2000, *MNRAS*, 317, 697
- Ferlet, R., Vidal-Madjar, A., & Gry, C. 1985, *ApJ*, 298, 838
- Forster, K., Rich, R. M., & McCarthy, J. K. 1995, *ApJ*, 450, 74
- Franx, M., & Illingworth, G. 1990, 359, L41
- Frye, B., Broadhurst, T., & Benítez, N. 2002, *ApJ*, in press
- Genzel, R., et al. 1998, *ApJ*, 498, 579
- Genzel, R., Tacconi, L. J., Rigopoulou, D., Lutz, D., & Tecza, M. 2001, *ApJ*, submitted (astro-ph/0106032)
- Goodrich, R. W., & Veilleux, S. 1988, *PASP*, 100, 1572
- González Delgado, R. M., Leitherer, C., Heckman, T., Lowenthal, J. D., Ferguson, H. C., & Robert, C. 1998, *ApJ*, 495, 698
- Hamilton, D., & Keel, W. C. 1987, *ApJ*, 321, 211
- Hamann, F., Barlow, T. A., Junkkarinen, V., & Burbidge, E. M. 1997, *ApJ*, 478, 80
- Heckman, T. M., Balick, B., & Crane, P. C. 1980, *A&AS*, 40, 295
- Heckman, T. M., Armus, L., & Miley, G. K. 1990, *ApJS*, 74, 833

- Heckman, T. M., & Leitherer, C. 1997, *AJ*, 114, 69
- Heckman, T. M., Lehnert, M. D., Strickland, D. K., & Armus, L. 2000, *ApJS*, 129, 493
- Heckman, T. M., Sembach, K. R., Meurer, G. R., Strickland, D. K., Martin, C. L., Calzetti, D., & Leitherer, C. 2001, *ApJ*, 554, 1021
- Herbig, G. H. 1993, *ApJ*, 407, 142
- Hobbs, L. M. 1974a, *ApJ*, 188, L107
- Hobbs, L. M. 1974b, *ApJ*, 191, 381
- Hobbs, L. M. 1976, *ApJ*, 203, 143
- Hudson, M. J., Lucey, J. R., Smith, R. J., & Steel, J. 1997, *MNRAS*, 291, 488
- Hughes, D. H., et al. 1998, *Nature*, 394, 241
- Hutchings, J. B., & Neff, S. G. 1987, *AJ*, 92, 14
- Jenkins, E. B. 1986, *ApJ*, 304, 739
- Jørgensen, I., Franx, M., & Kjaergaard, P. 1996, *MNRAS*, 280, 167
- Kauffmann, G., & Charlot, S. 1998, *MNRAS*, 294, 705
- Kawara, K., et al. 1998, *A&A*, 336, L9
- Kennicutt, R. C. 1998, *ApJ*, 498, 541
- Kim, D.-C., & Sanders, D. B. 1998, *ApJS*, 119, 41
- Kim, D.-C., Veilleux, S., & Sanders, D. B. 1998, *ApJ*, 484, 92
- Kriss, G. A. 1994, in *ASP Conf. Ser. 61, ADASS III*, ed. D. R. Crabtree, R. J. Hanisch, & J. Barnes (San Francisco: ASP), 437
- Kunth, D., Mas-Hesse, J. M., Terlevich, E., Terlevich, R., Lequeux, J., & Fall, S. M. 1998, *A&A*, 334, 11
- Larson, R. B. 1974, *MNRAS*, 169, 229
- Laureijs, R. J., et al. 2000, *A&A*, 359, 900
- Leitherer, C., & Heckman, T. M. 1995, *ApJS*, 96, 9

- Lequeux, J., Kunth, D., Mas-Hesse, J. M., & Sargent, W. L. W. 1995, *A&A*, 301, 18
- Lutz, D., Veilleux, S., & Genzel, R. 1999, *ApJ*, 517, L13
- Mac Low, M.-M., & Ferrara, A. 1999, *ApJ*, 513, 142
- Madau, P., Haardt, F., & Rees, M. J. 1999, *ApJ*, 514, 648
- Madau, P., Ferrara, A., & Rees, M. J. 2001, *ApJ*, 555, 92
- Martin, C. L. 1998, *ApJ*, 506, 222
- Martin, C. L. 1999, *ApJ*, 513, 156
- Matsuhara, H., et al. 2000, *A&A*, 361, 407
- Meurer, G. R., Heckman, T. M., Lehnert, M. D., Leitherer, C., & Lowenthal, J. 1997, *AJ*, 114, 54
- Mirabel, I. F., & Sanders, D. B. 1989, *ApJ*, 340, L53
- Morton, D. C. 1974, *ApJ*, 193, L35
- Morton, D. C. 1975, *ApJ*, 197, 85
- Morton, D. C. 1991, *ApJS*, 77, 119
- Murphy, T. W., Jr., Soifer, B. T., Matthews, K., & Armus, L. 2001, *ApJ*, 559, 201
- Nath, B. B., & Trentham, N. 1997, *MNRAS*, 291, 505
- Oey, M. S., Clarke, C. J., & Massey, P. 2001, in *Dwarf Galaxies and their Environment*, ed. K. de Boer, R. J. Dettmar, & U. Klein (Aachen: Shaker Verlag), 181
- Perault, M. 1987, Ph.D. thesis, Univ. Paris
- Pettini, M., Steidel, C. C., Adelberger, K. L., Dickinson, M., & Giavalisco, M. 2000, *ApJ*, 528, 96
- Pettini, M., Shapley, A. E., Steidel, C. C., Cuby, J.-G., Dickinson, M., Moorwood, A. F. M., Adelberger, K. L., & Giavalisco, M. 2001, *ApJ*, 554, 981
- Phillips, A. C. 1993, *AJ*, 105, 486
- Phillips, A. M., Pettini, M., & Gondhalekar, P. M. 1984, *MNRAS*, 206, 337

- Ponman, T. J., Cannon, D. B., & Navarro, J. F. 1999, *Nature*, 397, 135
- Puget, J. L., et al. 1999, *A&A*, 345, 29
- Rand, R. J. 1996, *ApJ*, 462, 712
- Rudy, R. J., Foltz, C. B., & Stocke, J. T. 1985, 288, 531
- Sahu, M. S., & Blades, J. C. 1997, *ApJ*, 484, L125
- Sanders, D. B., Scoville, N. Z., & Soifer, B. T. 1991, *ApJ*, 370, 158
- Sanders, D. B., & Mirabel, I. F. 1996, *ARA&A*, 34, 749
- Sanders, D. B. 1999, *Ap&SS*, 269, 381
- Savage, B. D., & Sembach, K. R. 1991, *ApJ*, 379, 245
- Savage, B. D., & Sembach, K. R. 1996, *ARA&A*, 34, 279
- Scannapieco, E., Ferrara, A., & Broadhurst, T. 2000, *ApJ*, 536, L11
- Scannapieco, E., & Broadhurst, T. 2001, *ApJ*, 549, 28
- Scannapieco, E., Thacker, R. J., & Davis, M. 2001, *ApJ*, 557, 605
- Serjeant, S., et al. 2001, *MNRAS*, 322, 262
- Shopbell, P. L., & Bland-Hawthorn, J. 1998, *ApJ*, 493, 129
- Silich, S., & Tenorio-Tagle, G. 2001, *ApJ*, 552, 91
- Smail, I., Ivison, R. J., & Blain, A. W. 1997, *ApJ*, 490, L5
- Soifer, B. T., et al. 2000, *AJ*, 119, 509
- Spitzer, L. 1978, *Physical Processes in the Interstellar Medium* (New York: Wiley-Interscience)
- Steidel, C. C., Pettini, M., & Adelberger, K. L. 2001, *ApJ*, 546, 665
- Stokes, G. M. 1978, *ApJS*, 36, 115
- Strickland, D. K. 2002, in *ASP Conf. Ser. 253*, “Chemical Enrichment of Intracluster and Intergalactic Medium,” (San Francisco: ASP)
- Terlevich, E., Díaz, A. I., & Terlevich, R. 1990, *MNRAS*, 242, 271

- Trentham, N., Blain, A. W., & Goldader, J. 1999, MNRAS, 305, 61
- Vader, J. P. 1986, ApJ, 305, 669
- Veilleux, S., Cecil, G., Bland-Hawthorn, J., Tully, R. B., Filippenko, A. V., & Sargent, W. L. W. 1994, ApJ, 433, 48
- Veilleux, S., Kim, D.-C., Sanders, D. B., Mazzarella, J. M., & Soifer, B. T. 1995, ApJS, 98, 171
- Veilleux, S., Kim, D.-C., & Sanders, D. B. 1999a, ApJ, 522, 113
- Veilleux, S., Sanders, D. B., & Kim, D.-C. 1999b, ApJ, 522, 139
- Veilleux, S., & Rupke, D. S. 2002, ApJ, 565, L63
- Veilleux, S., Kim, D.-C., Sanders, D. B., & Rupke, D. S. 2002, ApJ, submitted

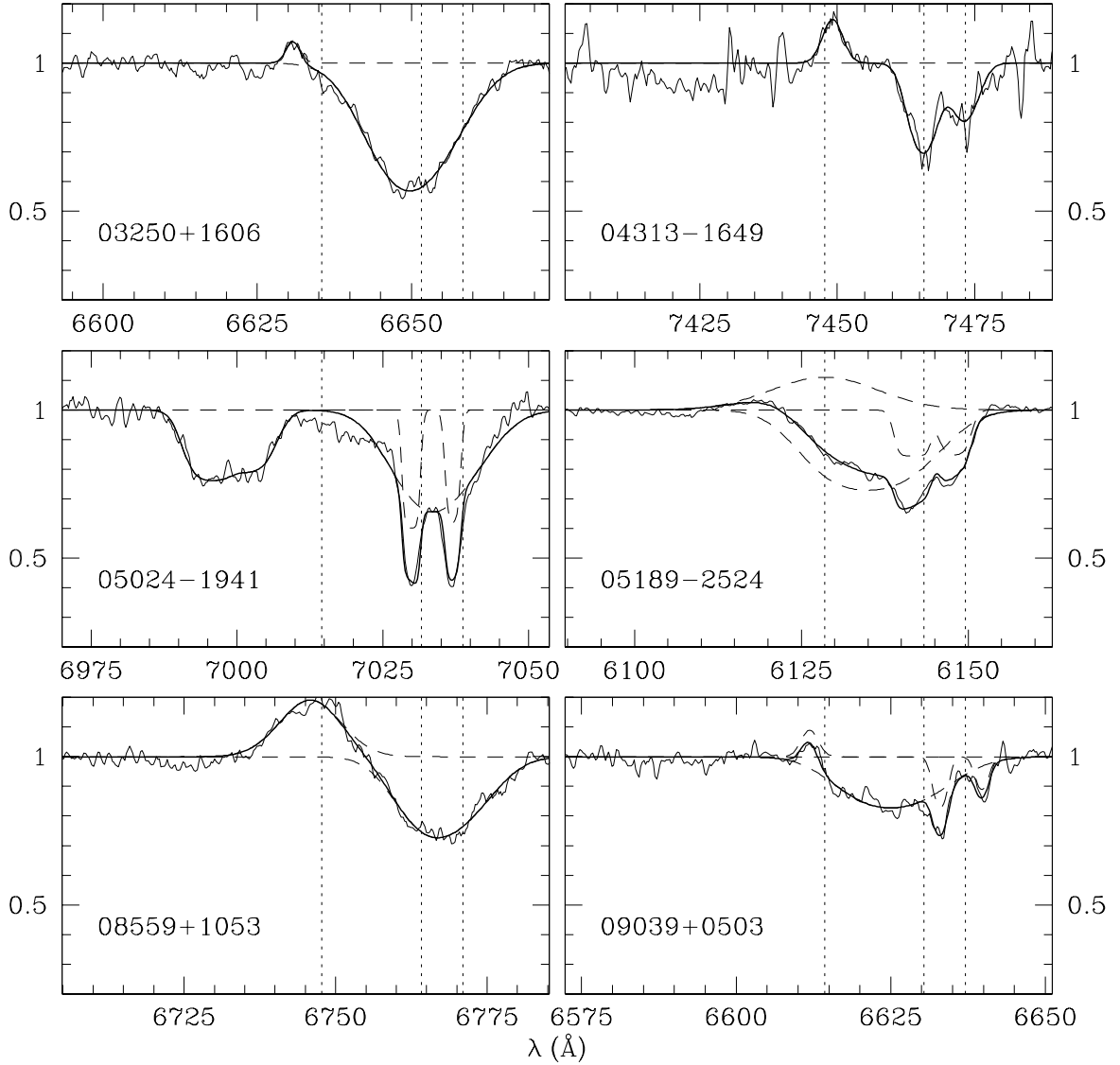


Fig. 1.— Spectra of the Na I D line in our 11 program objects. The thin, jagged, solid lines are the original spectra smoothed with a boxcar of width 3 pixels, and the thick, smooth, solid lines are the fits to the data. The dashed lines indicate the individual components of the fit. The vertical dotted lines locate the Na I D doublet and He I λ 5876 line in the rest frame of the galaxy.

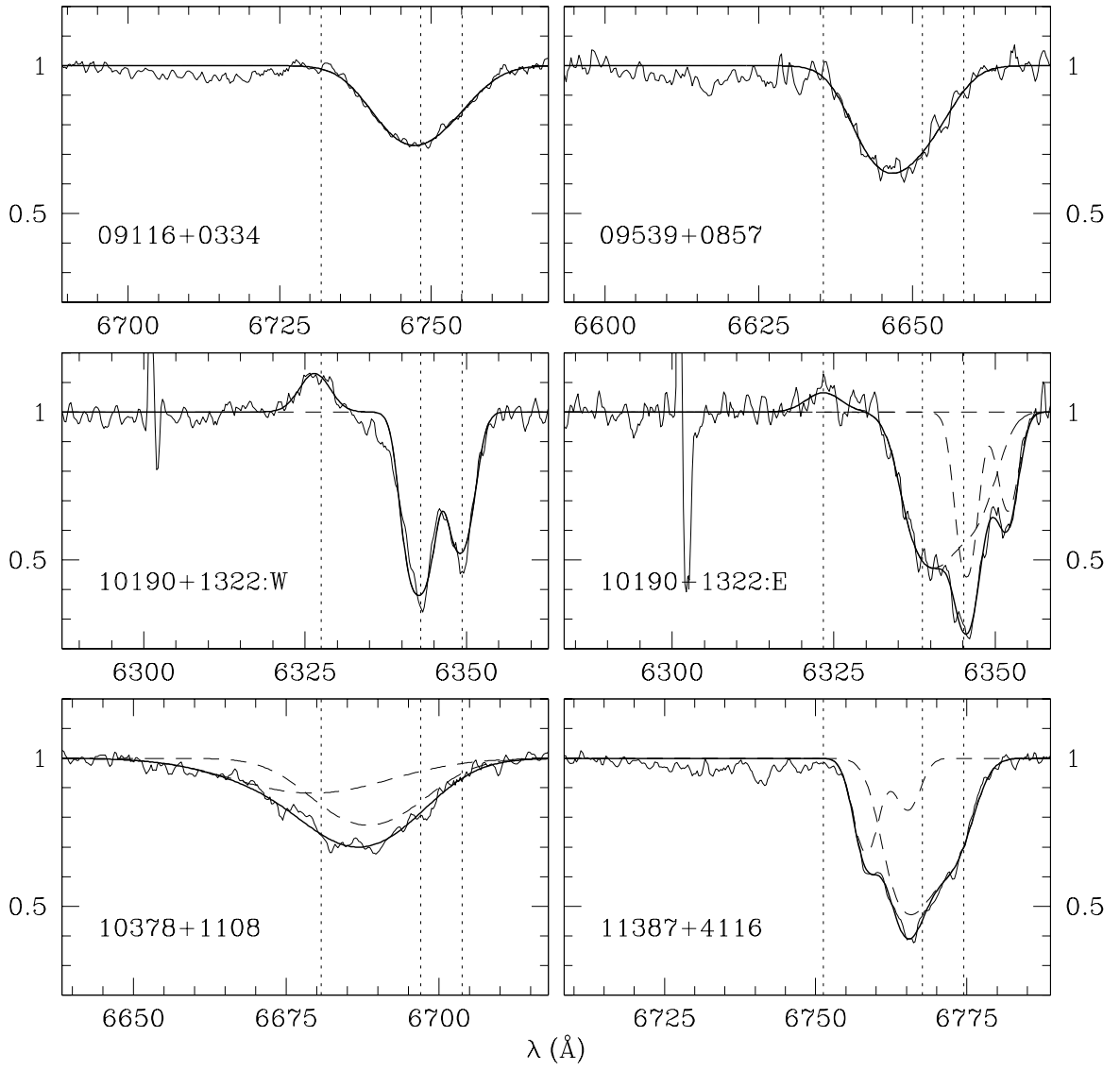


Fig. 1.— *Continued.*

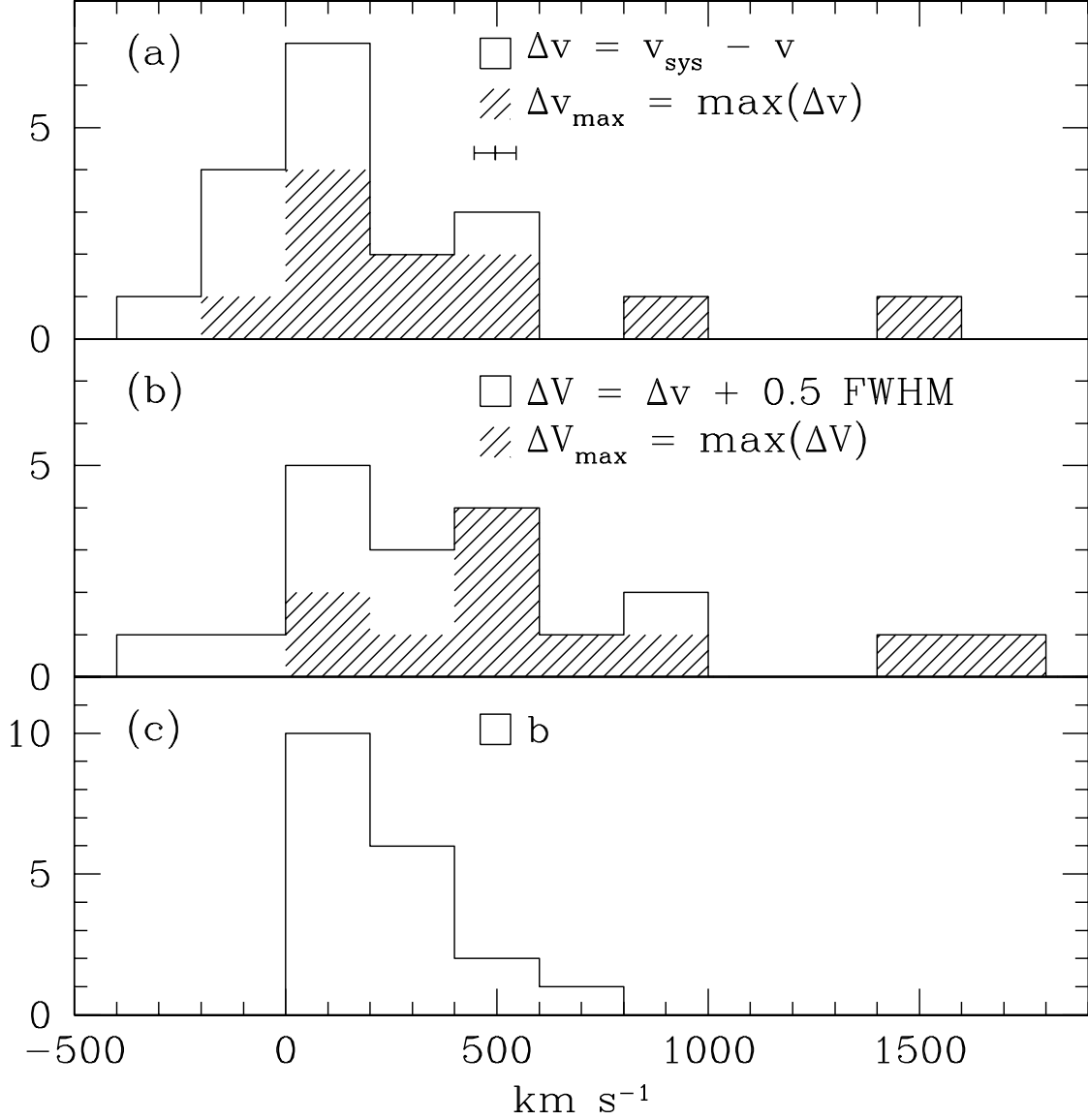


Fig. 2.— Distributions of various kinematic quantities: (a) velocity relative to systemic for each component, $\Delta v = v_{\text{sys}} - v$, unshaded; and maximum Δv for each object, $\Delta v_{\text{max}} = \max(\Delta v)$, shaded; (b) highest velocity within each component, $\Delta V = \Delta v + \frac{1}{2}\text{FWHM}$, unshaded; and maximum ΔV for each object, $\Delta V_{\text{max}} = \max(\Delta V)$, shaded; and (c) Doppler parameter b for each component. Note that blueshifted velocities are positive, and that FWHM (and thus b) is corrected in quadrature for a 65 km s^{-1} instrumental resolution. The error bar in (a) represents a typical $\sim 2\text{-}3 \sigma$ uncertainty.

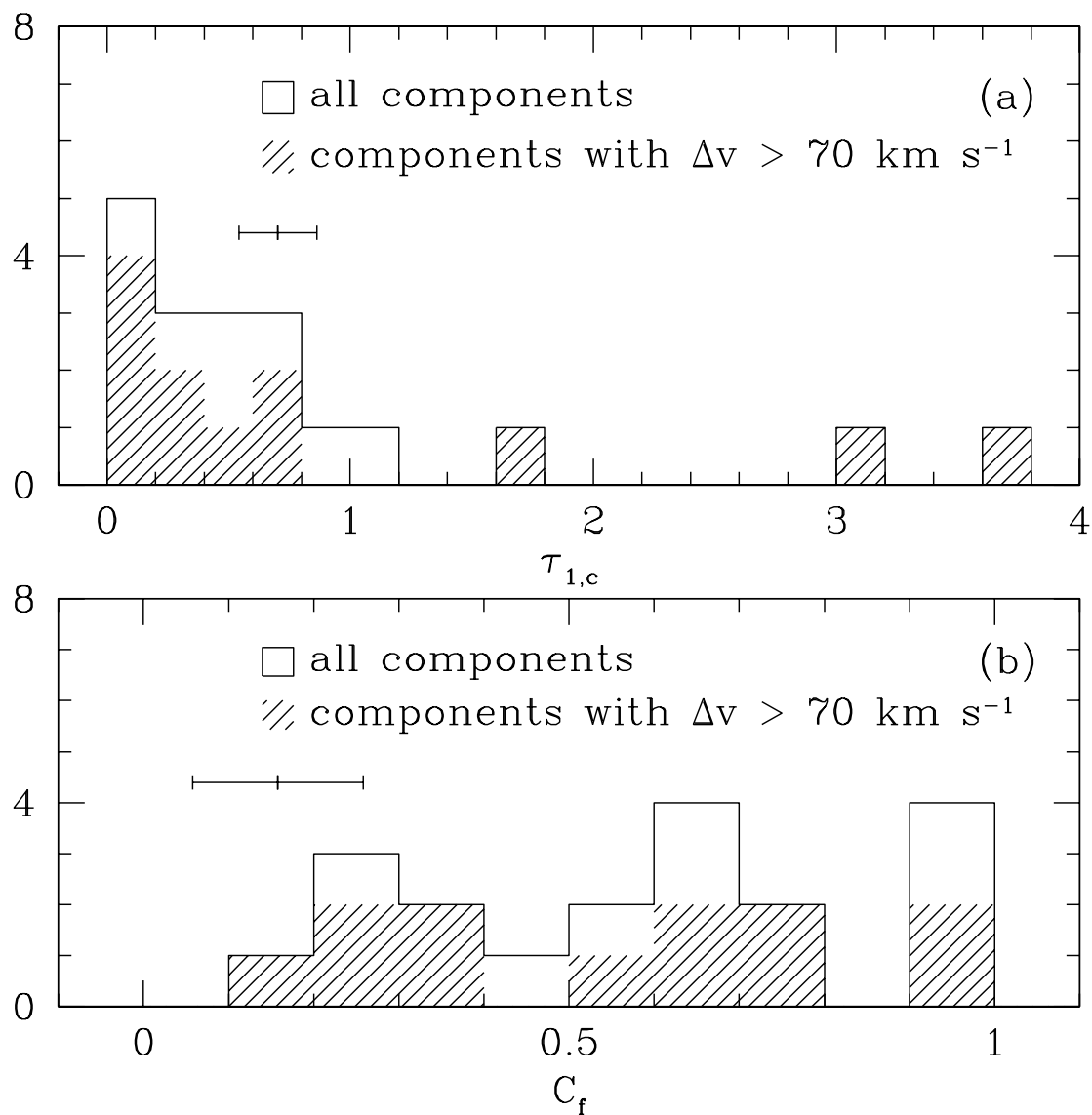


Fig. 3.— Distributions of (a) central optical depth $\tau_{1,c}$ of the Na I D₁ $\lambda 5896$ line and (b) covering fraction C_f . Unshaded histograms include all components; shaded histograms include only components with $\Delta v > 70 \text{ km s}^{-1}$ (i.e. those assumed to be outflowing). The error bars represent typical $\sim 2\text{-}3 \sigma$ uncertainties.

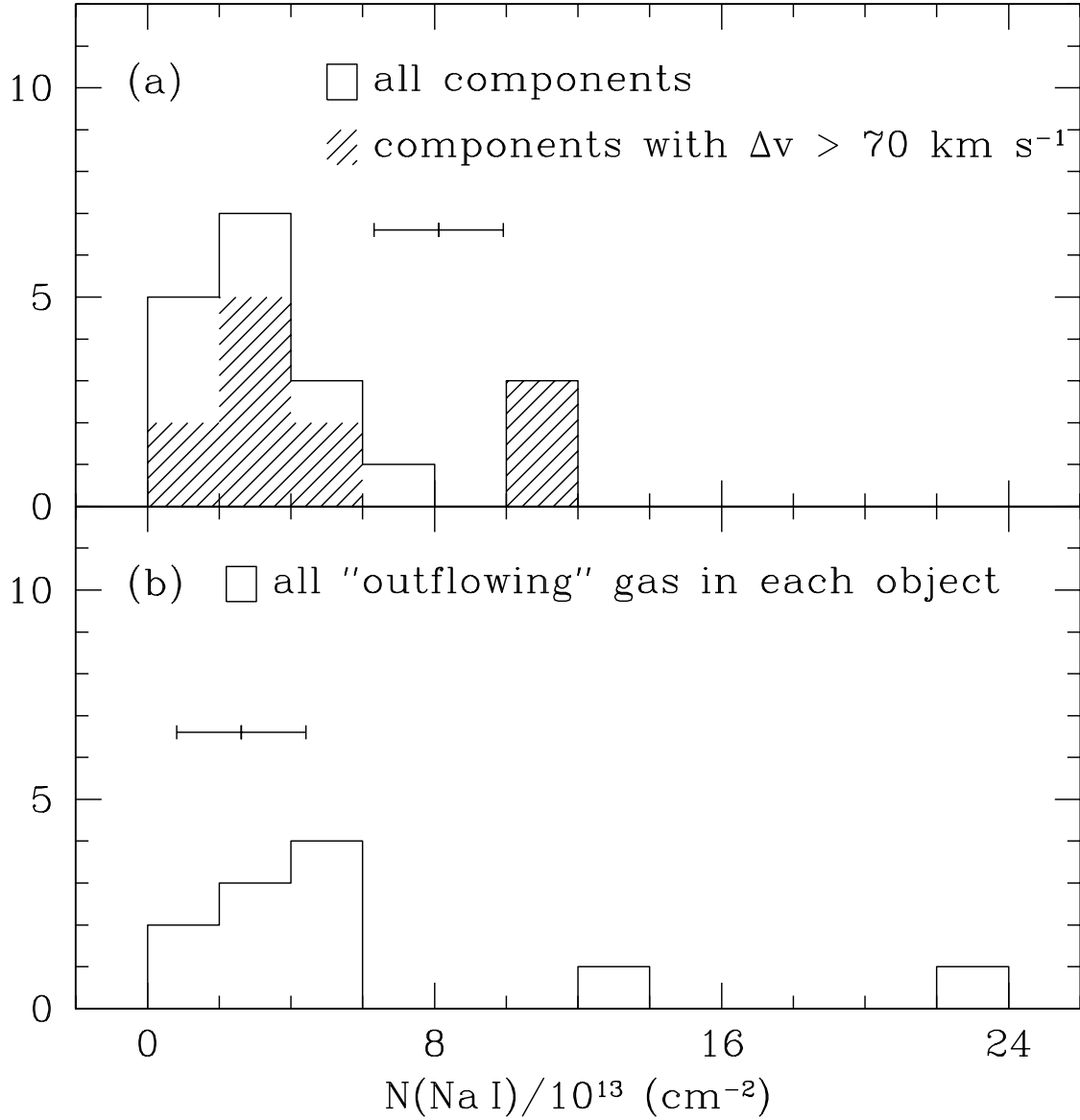


Fig. 4.— Distributions of (a) column density of Na I for each component (unshaded) and only components with $\Delta v > 70 \text{ km s}^{-1}$ (shaded) and (b) total column density of Na I gas assumed to be outflowing in each object. The error bars represent typical $\sim 2\text{-}3 \sigma$ uncertainties.

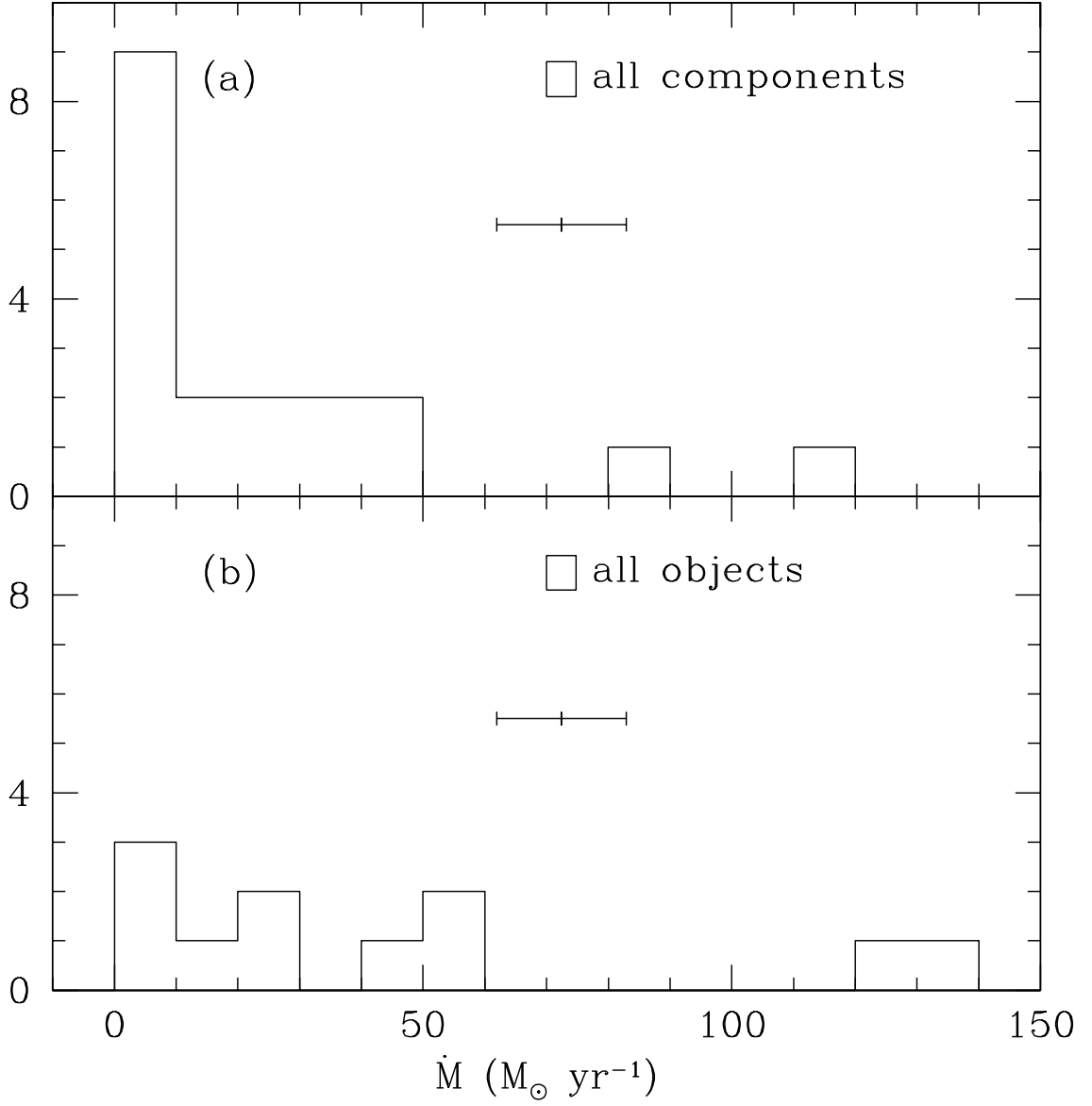


Fig. 5.— Distributions of (a) mass outflow rate \dot{M} for each component and (b) total mass outflow rate \dot{M}_{tot} for each object. The error bars represent typical $\sim 2\text{-}3 \sigma$ uncertainties.

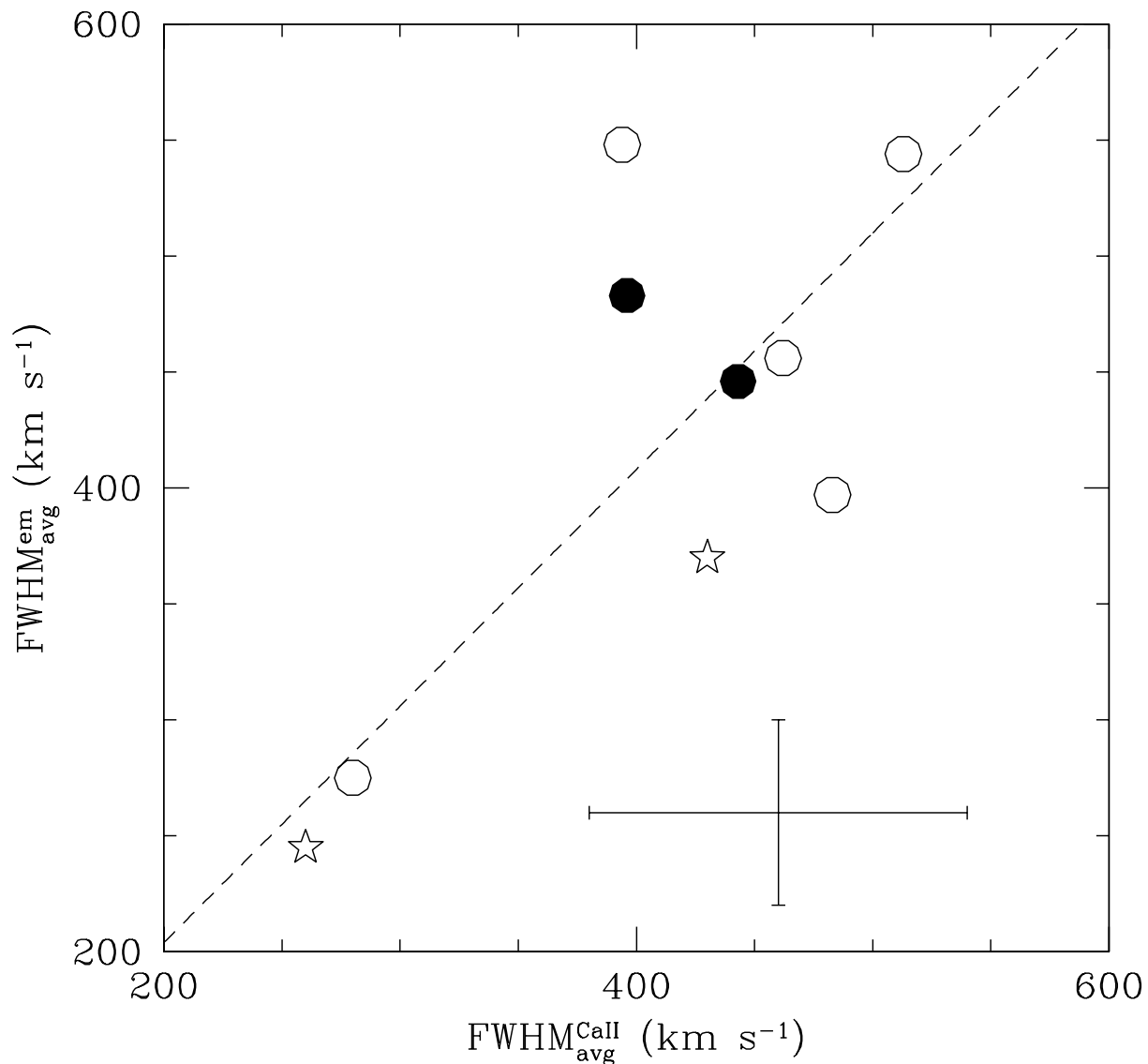


Fig. 6.— Average emission line FWHM vs. average FWHM of Ca II triplet absorption feature ($\lambda\lambda 8498, 8542, 8662$). The two quantities correlate; a linear regression yields $\text{FWHM}_{\text{avg}}^{\text{em}} = (1.02 \pm 0.06) \times \text{FWHM}_{\text{avg}}^{\text{CaII}}$, with a correlation coefficient of 0.99. The dashed line is the fit. Symbols denote optical spectral type: open star = H II-region-like object; open circle = LINER; filled circle = Seyfert 2. The error bars represent typical $\sim 2\text{-}3 \sigma$ uncertainties.

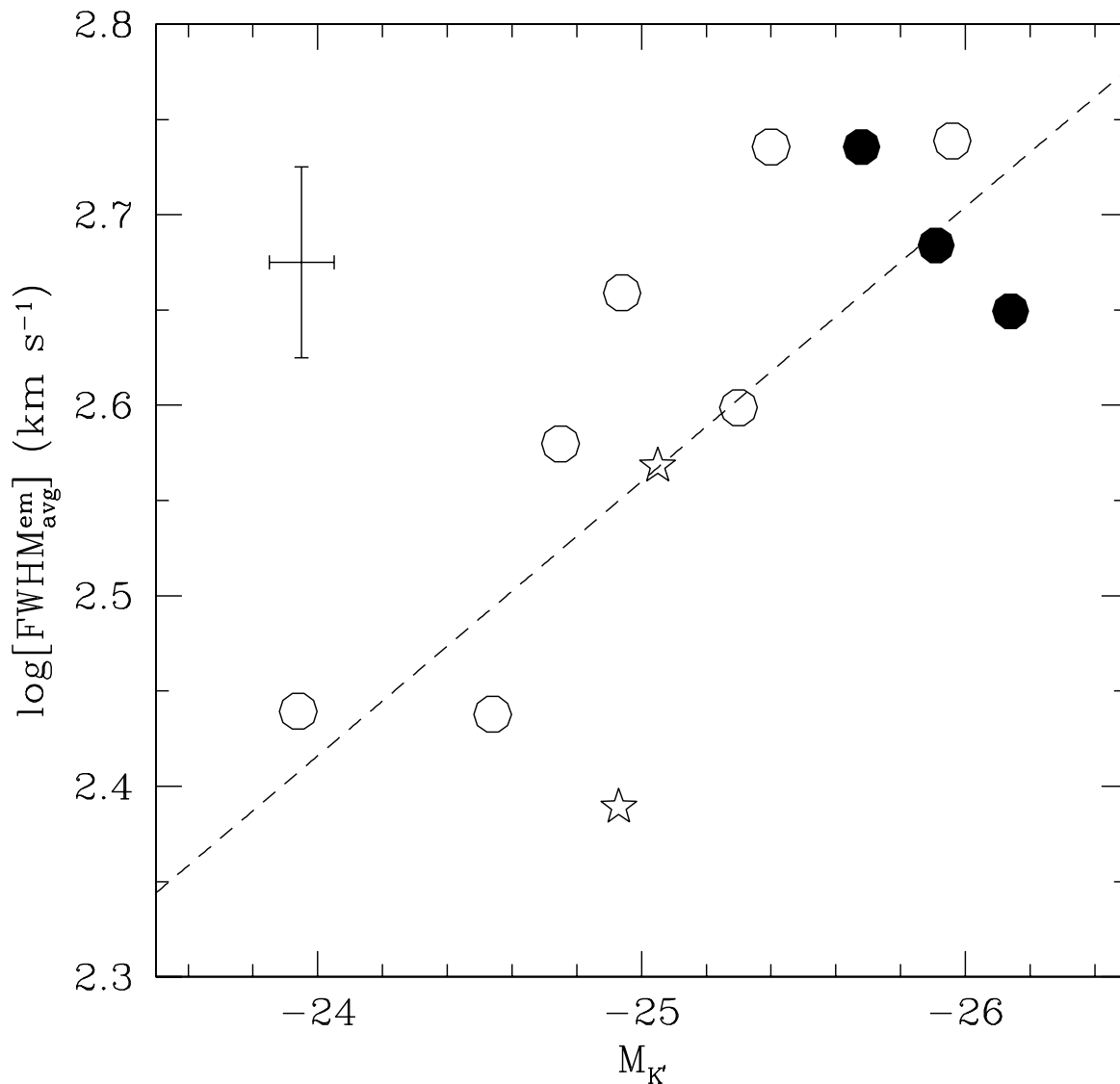


Fig. 7.— Logarithm of average emission line FWHM vs. absolute K' -band magnitude. Dashed lines indicate the fit; a linear regression yields $\log[\text{FWHM}_{\text{avg}}^{\text{em}}] = (0.14 \pm 0.04) M_{K'} - (1.04 \pm 0.98)$ with a correlation coefficient of 0.76. As in Fig. 6, symbol shapes denote optical spectral type. The error bars represent typical $\sim 2\text{-}3\sigma$ uncertainties.

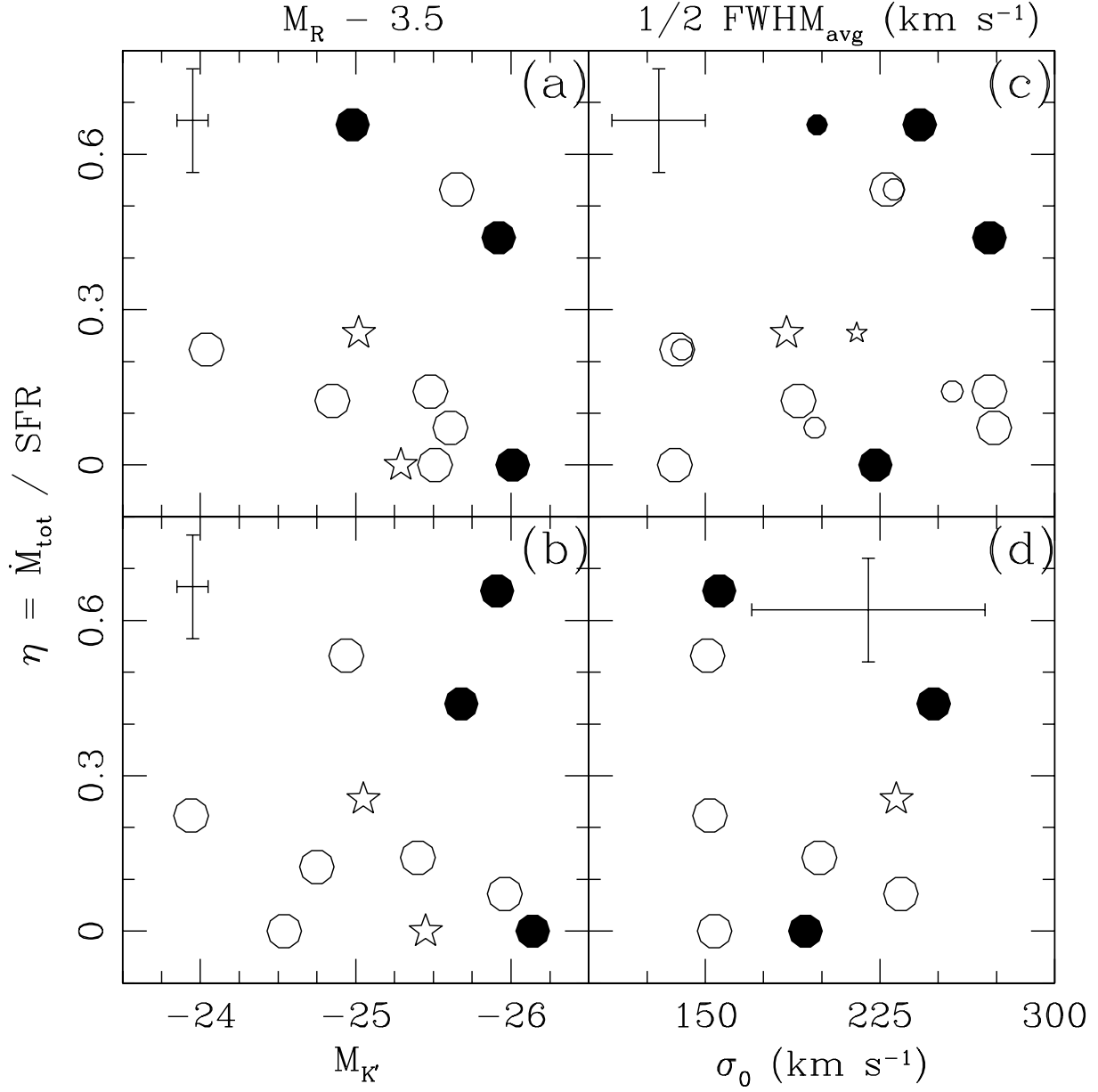


Fig. 8.— Reheating efficiency $\eta = \dot{M}/\text{SFR}$ vs. various quantities: (a) absolute R -band magnitude; (b) absolute K' -band magnitude; (c) one-half the average emission-line FWHM (large symbols) and Ca II triplet FWHM (small symbols); and (d) the central velocity dispersion computed from the fundamental plane. There appear to be no correlations for the entire sample or any one spectral type. As in previous figures, symbol shapes denote optical spectral type. The error bars represent typical $\sim 2\text{-}3\sigma$ uncertainties.

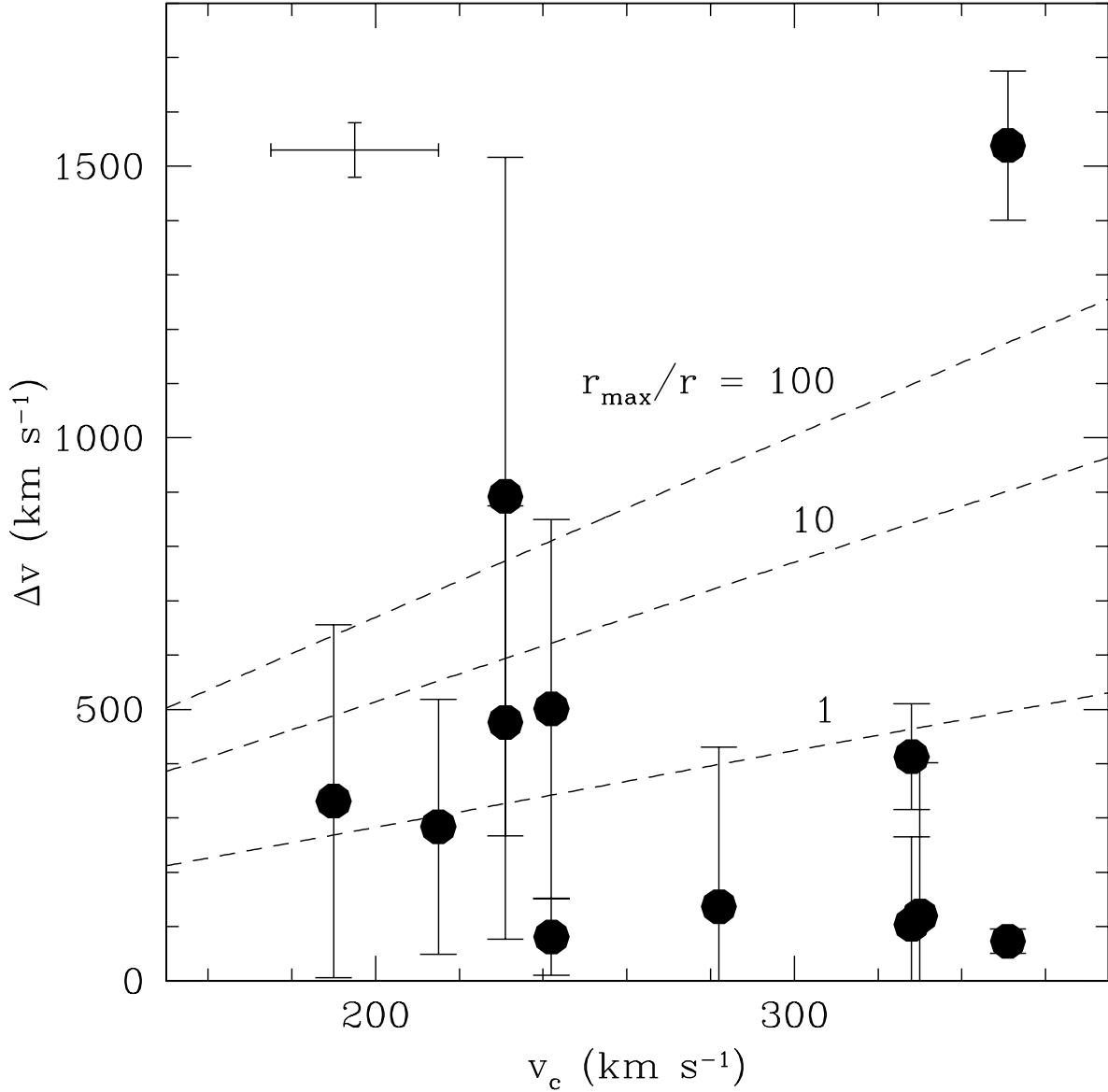


Fig. 9.— Velocity relative to systemic of each component assumed to be outflowing vs. estimated circular velocity of host galaxy. The vertical bar on each point represents the FWHM of the corresponding fitted profile in velocity space. The dotted lines are values of v_{esc} for a singular isothermal sphere truncated at r_{\max} , for various values of r_{\max}/r . Profiles that extend above a given value of v_{esc} may represent escaping material. We adopt $r_{\max}/r = 10$ in the text, but the average escape fraction in the sample is not sensitive to this quantity. The cross in the upper left-hand corner represents measurement uncertainties for Δv and $\frac{1}{2}\text{FWHM}_{\text{avg}}^{\text{em}}$; if $\frac{1}{2}\text{FWHM}_{\text{avg}}^{\text{CaII}}$ or σ_0 are used to determine v_c , the errors are larger.

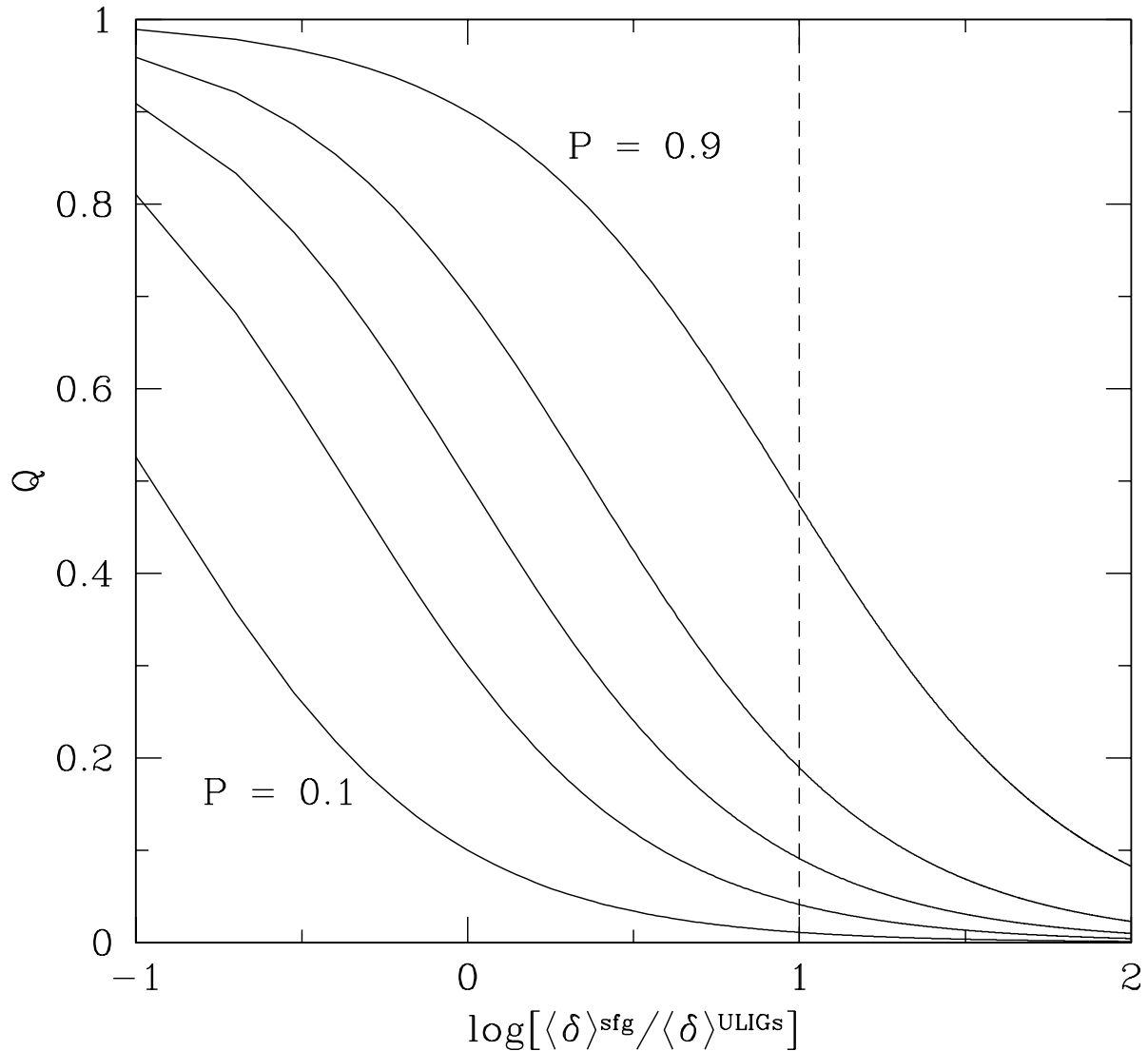


Fig. 10.— Fraction of gas being injected into the IGM that originates in ULIGs, Q , as a function of the ratio of the average ejection efficiency of all other star-forming galaxies to that in ULIGs. The different lines represent different values of P , the fractional contribution of ULIGs to the total star formation rate density of the universe at a given z , in steps of 0.2. The vertical dotted line indicates $\langle \delta \rangle^{\text{sfg}} / \langle \delta \rangle^{\text{ULIGs}} = 10$, which matches current measurements. Note that in this case $Q \gtrsim 0.1$ only if $P \gtrsim 0.5$.

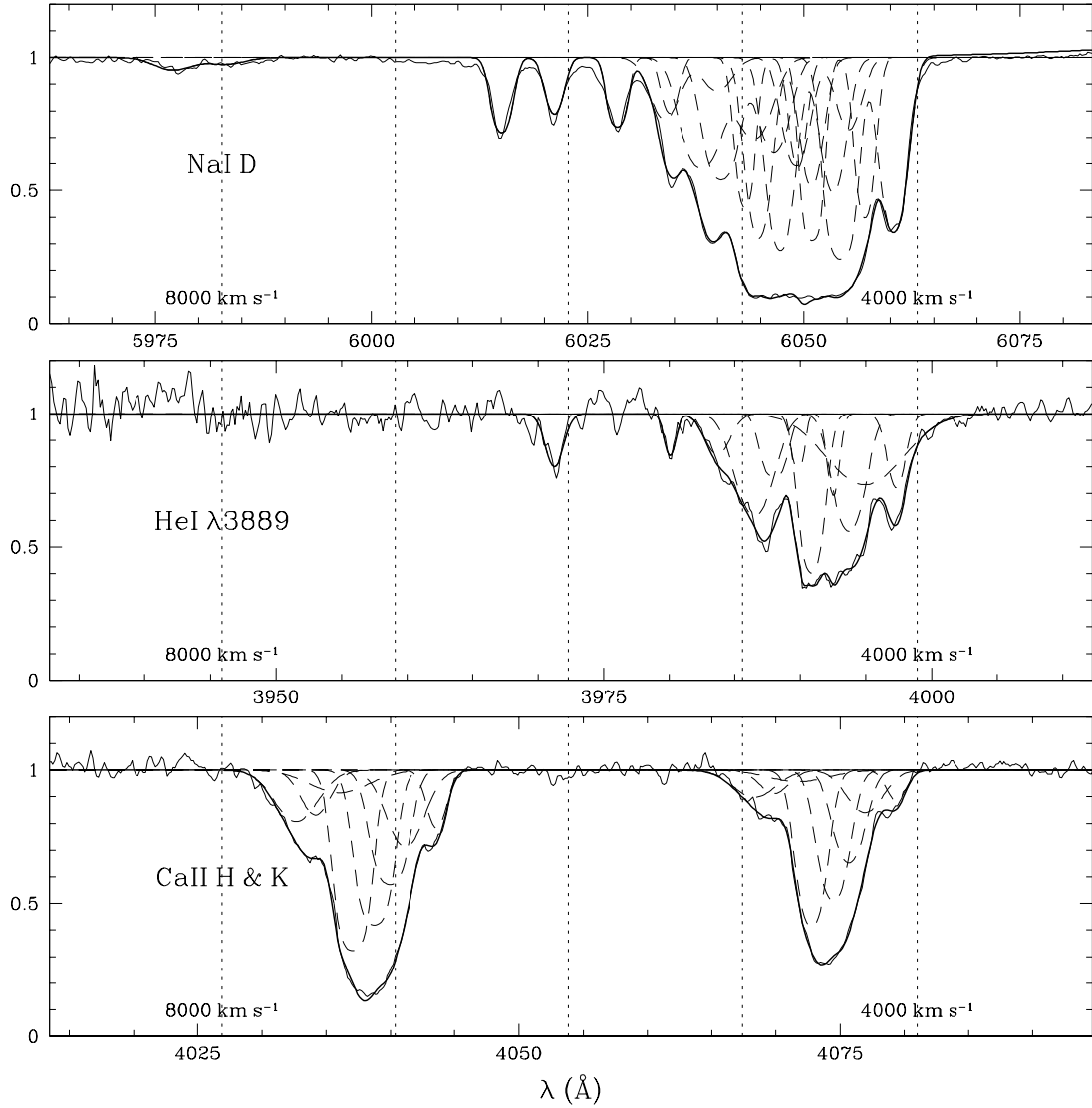


Fig. 11.— Spectra of absorption lines in Mrk 231. As in Fig. 1, thin solid lines indicate the data, thick solid lines indicate the model, and dashed lines indicate the model components. The vertical dotted lines are lines of constant blueshifted velocity relative to systemic, spaced at intervals of 1000 km s^{-1} , for Na I D $\lambda 5896$, He I $\lambda 3889$, and Ca II H $\lambda 3968$.

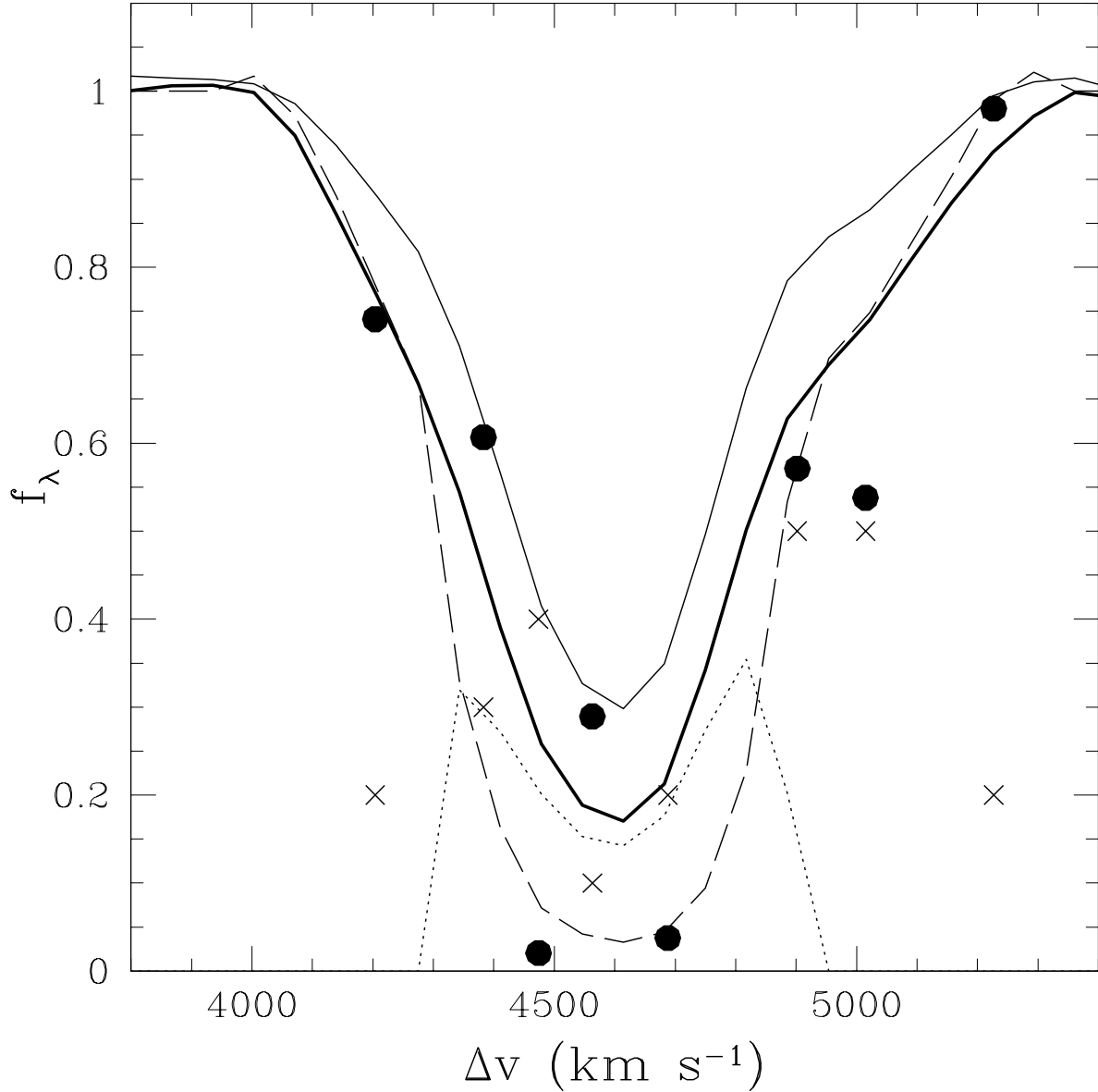


Fig. 12.— Ca II H & K lines in Mrk 231, plotted as a function of blueshifted velocity relative to systemic. The solid lines represent the data, binned in velocity space by 68 km s^{-1} and boxcar smoothed over 3 bins. The thin line is Ca II H $\lambda 3968$ and the thick line is Ca II K $\lambda 3934$. The dotted line is $(1 - C_f)$, where C_f is the covering fraction as a function of velocity. Finally, the dashed line is $e^{-2\tau_1}$, where τ_1 is the optical depth of Ca II H. The circles and crosses denote the values of $1 - C_f$ and $e^{-2\tau_1}$ that we derive using our curve-of-growth fitting method. Note that at high optical depths (i.e. near line center) C_f is smaller and the line intensity is largely determined by C_f , rather than τ .

Table 1. Sample Properties

IRAS FSC (1)	z (2)	$\log(\frac{L_{\text{IR}}}{L_{\odot}})$ (3)	Type (4)	$M_{K'}$ (5)	M_R (6)	r_e (7)	μ_e (8)	Date (9)	Seeing (10)	Exp. Time (11)
03250+1606	0.1289	12.06	L	-25.40	-21.98	5.1	21.2	2	0.9	2×900
04313–1649	0.2672	12.55	L	-24.54	-22.01	6.2	21.8	3	0.8	2×1200
05024–1941	0.1935	12.43	S2	-25.68	-22.42	4.7	20.8	2	0.9	2×900
05189–2524	0.04274	12.07	S2	-25.91	-21.48	4.3	21.3	3	0.8	900
08559+1053	0.1481	12.16	S2	-26.14	-22.51	6.2	21.5	1	1.1	1200
09039+0503	0.1254	12.07	L	-24.75	-21.35	2	0.9	2×900
09116+0334	0.1454	12.11	L	-25.96	-22.11	4.1	20.7	1	1.1	1200
09539+0857	0.1290	12.03	L	-23.94	-20.54	3.1	20.9	2	0.9	2×900
10190+1322:W	0.0766	12.00 ^a	H	-24.93 ^a	-21.69 ^a	2	0.9	900
10190+1322:E	0.0759		L	-25.30 ^a	-21.09 ^a	2	0.9	900
10378+1108	0.1367	12.26	L	-24.94	-22.15	6.1	21.8	3	0.8	2×900
11387+4116	0.1487	12.18	H	-25.05	-21.52	3.5	20.5	3	0.8	2×900
12540+5708 ^b	0.04217	12.50	S1	-27.08	-22.52	3.3	19.8	3	0.8	300

Note. — Col.(1): Target name. FSC = Faint Source Catalog. Col.(2): Redshift; see Table 4. Col.(3): Infrared luminosity, computed from a single-temperature dust-emissivity fit to the fluxes in all four IRAS bands; see Perault 1987 or Sanders & Mirabel 1996. Col.(4): Optical spectral type. H = H II-region-like, L = LINER, S1 = Seyfert 1, S2 = Seyfert 2. From Veilleux, Kim, & Sanders 1999a, except for F04313 – 1649 and F10190 + 1322, for which we used the present dataset. Col.(5): K' -band absolute magnitude, from Veilleux et al. 2002. Col.(6): R -band absolute magnitude, from Veilleux et al. 2002. Col.(7): Effective radius from R -band surface brightness profile, in kpc. From Veilleux et al. 2002. Col.(8): Surface brightness inside r_e , in mag arcs⁻². From Veilleux et al. 2002. Col.(9): UT date of observation. 1 = 2001 Jan 24, 2 = 2001 Feb 27, 3 = 2001 Feb 28. Col.(10): Average seeing on the date of observation, in arcseconds. Col.(11): Exposure time, in seconds.

^aF10190 + 1322 has two nuclei separated by 6.2 kpc. L_{IR} refers to the object as a whole, i.e. both nuclei at once. The values of $M_{K'}$ and M_R for each nucleus are scaled from the values for the object as a whole ($M_{K'} = -25.45$ and $M_R = -21.79$) using the absolute magnitudes within 2 kpc of each nucleus.

^bMrk 231

Table 2. Measured Properties of Na I D Lines

IRAS FSC (1)	No. (2)	λ_1 (3)	$\tau_{1,c}$ (4)	b (5)	C_f (6)	R (7)	$W_{\text{eq}}^{\text{rest}}$ (8)	% (9)
03250+1606	1	6654.7	0.22	353	1.00	1.86	6.7	14
04313–1649	1	7473.2	0.58	124	0.44	1.68	2.5	15
05024–1941	1	7002.7	1.72	165	0.25	1.38	9.7	4
	2	7037.0	3.14	27	0.40	1.24		
	3	7038.9	0.17	333	1.00	1.89		
05189–2524	1	6139.4	0.73	419	0.31	1.62	5.5	12
	2	6148.0	3.75	85	0.16	1.21		
08559+1053	1	6772.2	0.27	313	0.56	1.83	3.9	19
09039+0503	1	6629.8	0.42	390	0.26	1.75	3.5	28
	2	6639.7	0.63	50	0.24	1.66		
09116+0334	1	6752.4	0.18	338	0.72	1.88	3.9	18
09539+0857	1	6652.0	0.36	282	0.62	1.78	4.9	16
10190+1322:W	1	6349.0	1.20	114	0.68	1.48	6.1	15
10190+1322:E	1	6346.4	0.92	200	0.61	1.56	9.1	10
	2	6352.0	0.41	94	1.00	1.76		
10378+1108	1	6683.8	0.06	750	0.77	1.96	7.3	11
	2	6693.1	0.17	479	0.60	1.89		
11387+4116	1	6765.2	0.19	117	1.00	1.88	8.0	14
	2	6772.2	0.74	194	0.67	1.62		

Note. — Col.(1): Target name. Col.(2): Component number. Components listed in order from highest to lowest velocity relative to systemic. Col.(3): Centroid of D₁ λ 5896 line, in Å. Col.(4): Central optical depth of D₁ line. Optical depth of D₂ λ 5890 is twice this value. Col.(5): Doppler parameter of absorbing gas in km s^{−1}, equal to FWHM/(2 $\sqrt{\ln 2}$). Before conversion to b , the FWHM is corrected in quadrature for a 65 km s^{−1} instrumental resolution. Col.(6): Covering fraction of absorbing gas. Col.(7): Doublet equivalent width ratio $R = W_{\text{eq}}^{\lambda 5890} / W_{\text{eq}}^{\lambda 5896}$. Col.(8): Total rest-frame equivalent width of Na I D absorption complex, in Å. The rest-frame equivalent width is related to the observed equivalent width by $W_{\text{eq}}^{\text{rest}} = W_{\text{eq}}^{\text{obs}} / (1 + z)$. Col.(9): Percent stellar contribution to Na I D line, estimated from the equivalent width of the Mg I b triplet.

Table 3. Absorption Line Equivalent Widths

IRAS FSC	Mg I b	H γ	H δ	H8	H9	H10	H11	Ca II K	Ca II	Ca II	Ca II
(1)	(2)	(3)	(4)	(5)	(6)	(7)	(8)	(9)	(10)	(11)	(12)
03250+1606	1.9	10.4	8.9	9.0::	...	5.7	2.9::
04313-1649	0.8	6.2::	7.8	5.5	5.3::	3.2
05024-1941	0.7	3.3	...	8.6	7.8	4.7	...	3.2
05189-2524	1.3	4.1	5.7	5.7	6.4	6.0	...	1.9	1.1	2.0	2.0
08559+1053	1.4	3.2	3.9	2.2::	...
09039+0503	2.0	6.2::	5.9	2.9::	3.1
09116+0334	1.4	...	7.9	7.9	7.4	5.2	1.2	2.2	...
09539+0857	1.6	9.1	6.6	4.5	...	3.4	...	2.6::	2.1
10190+1322:W	1.8	7.4::	6.9	4.7::	...	3.5	2.3::	2.8	...
10190+1322:E	1.8	15.5::	17.5::	4.5	...	3.0	...
10378+1108	1.5	7.1	5.6	...	5.2	1.6::	3.8::	1.5
11387+4116	2.2	...	6.2	10.4	7.3	5.3	1.8	4.0	3.6::

Note. — Col.(1): Target name. Col.(2)-(12): Equivalent widths of selected absorption lines, in Å. Uncertainties are generally $\sim 20\%$; numbers marked with a (::) have an uncertainty of $\sim 40\%$. Values quoted are rest-frame equivalent widths: $W_{\text{eq}}^{\text{rest}} = W_{\text{eq}}^{\text{obs}}/(1+z)$. Wavelengths listed in the table header are wavelengths in air.

Table 4. Redshifts

IRAS FSC (1)	z_{abs} (2)	z_{em} (3)	z_{other} (4)	z_{adopt} (5)
03250+1606	0.1290	0.1289	...	0.1289
04313–1649	0.2672	0.2675	...	0.2672
05024–1941	0.1936	0.1935	0.1914 ^a	0.1935
05189–2524	0.0429	0.0427	0.04274 ^b	0.04274
08559+1053	0.1482	0.1480	...	0.1481
09039+0503	0.1254	0.1250	...	0.1254
09116+0334	0.1454	0.1453	...	0.1454
09539+0857	0.1290	0.1291	...	0.1290
10190+1322:W	0.0767	0.0766	...	0.0766
10190+1322:E	0.0758	0.0760	...	0.0759
10378+1108	0.1367	0.1363	...	0.1367
11387+4116	0.1487	0.1487	...	0.1487
12540+5708	0.04217 ^c	0.04217

Note. — Col.(1): Target name. Col.(2): Average redshift measured from stellar absorption lines, including as many as possible of the following lines: the Balmer lines $H\gamma - H10$, Ca II K, and the Ca II triplet. Col.(3): Average redshift measured from emission lines, including as many as possible of the following lines: the Balmer lines $H\alpha - H\delta$, [N II] $\lambda\lambda 6548, 6583$, [O III] $\lambda\lambda 4959, 5007$, [O I] $\lambda\lambda 6300, 6363$, [S II] $\lambda\lambda 6716, 6731$. (We also used He II $\lambda 4686$ and [Ni II] $\lambda 7378$ in a couple of objects.) Col.(4): Redshifts from other sources: CO, H I, and higher-excitation emission lines. Col.(5): Adopted redshift. CO and H I data are used where possible. In other cases, where the emission- and absorption-line redshifts differ by no more than $\Delta z = \pm 0.0002$, we take the average of the two. Otherwise, we use the absorption-line redshift.

^aRedshift measured from [O III] $\lambda\lambda 4959, 5007$, using this dataset.

^bRedshift measured from CO emission; see Sanders, Scoville, & Soifer 1991.

^cRedshift measured from H I absorption; see Carilli, Wrobel, & Ulvestad 1998.

Table 5. Computed Properties

IRAS FSC (1)	No. (2)	$N(\text{Na I})$ (3)	$N(\text{H})$ (4)	Δv (5)	ΔV (6)	\dot{M} (7)	\dot{M}_{tot} (8)	$\frac{\text{SFR}}{\alpha}$ (9)	α (10)	$\frac{\dot{M}_{\text{tot}}}{\text{SFR}}$ (11)	$\frac{\dot{M}_{\text{esc}}}{\dot{M}_{\text{tot}}}$ (12)	$\frac{\dot{M}_{\text{esc}}}{\text{SFR}}$ (13)
03250+1606	1	2.8	1.6	137	431	22	22	198	0.8	0.14	0.01	0.00
04313–1649	1	2.6	1.5	9	112	0.0	0	612	0.8	0.00	0.00	0.00
05024–1941	1	10	3.0	1538	1676	117	122	464	0.6	0.44	0.96	0.42
	2	3.0	1.7	73	96	5.0						
	3	2.0	1.4	-9	268	0.0						
05189–2524	1	11	3.1	501	849	49	53	203	0.4	0.66	0.31	0.21
	2	11	3.1	81	152	4.2						
08559+1053	1	3.0	1.7	-49	212	0.0	0	249	0.6	0.00	0.00	0.00
09039+0503	1	5.8	2.3	331	656	20	20	203	0.8	0.12	0.28	0.03
	2	1.1	1.0	-118	-77	0.0						
09116+0334	1	2.2	1.4	120	402	13	13	222	0.8	0.07	0.00	0.00
09539+0857	1	3.6	1.8	284	519	33	33	185	0.8	0.22	0.09	0.02
10190+1322:W	1	4.9	2.1	14	108	0.0	0 ^a	172 ^a	0.8 ^a	0.00 ^a	0.00 ^a	0.00 ^a
10190+1322:E	1	6.5	2.4	-58	109	0.0						
	2	1.4	1.2	-321	-243	0.0						
10378+1108	1	1.5	1.2	892	1517	85	133	314	0.8	0.53	0.58	0.31
	2	2.9	1.6	476	875	48						
11387+4116	1	0.80	0.89	413	511	38	53	261	0.8	0.26	0.00	0.00
	2	5.1	2.1	104	265	15						

Note. — Col.(1): Target name. Col.(2): Component number. Col.(3): Column density of Na I, in units of 10^{13} cm^{-2} . Col.(4): Column density of H, in units of 10^{21} cm^{-2} . Col.(5): Velocity of the component relative to systemic, in km s^{-1} : $\Delta v = v_{\text{sys}} - v$. Blueshifted velocities are positive. Col.(6): “Maximum” blueshifted velocity of the component, in km s^{-1} : $\Delta V = \Delta v + \frac{1}{2}\text{FWHM}$. Col.(7): Mass outflow rate for the component in $M_{\odot} \text{ yr}^{-1}$. Col.(8): Total mass outflow rate for the object in $M_{\odot} \text{ yr}^{-1}$. Col.(9): Star formation rate in $M_{\odot} \text{ yr}^{-1}$, derived from L_{IR} using the prescription in Kennicutt 1998 and parameterized by the fractional contribution of star formation to the infrared luminosity, which is given by α ($0 \leq \alpha \leq 1$). Col.(10): Estimated fraction of infrared (or \sim bolometric) luminosity powered by star formation. Col.(11): Reheating efficiency η , equal to the total mass outflow rate normalized by the corresponding global star formation rate, and including the proper values for α . Col.(12): Escape fraction f_{esc} , equal to the mass outflow rate of escaping gas divided by the total mass outflow rate. Col.(13): Ejection efficiency δ , equal to the total mass outflow rate of escaping gas normalized by the corresponding global star formation rate.

^aThe infrared luminosity L_{IR} for F10190 + 1322 refers to both nuclei, so these quantities also refer to the object as a whole.

Table 6. Na to H Conversion Factors

Ref.	β	γ	H ₂	$\frac{N_2(\text{H})}{N_1(\text{H})}$
(1)	(2)	(3)	(4)	(5)
1	2.3 ± 0.4	...	n	...
2	2.3	-35.1	n	5 – 24
3	2.1	...	b	...
4	2.11	-31.3	y	6 – 29
5	1.04 ± 0.08	-9.09	y	36 – 41
6	1.61 ± 0.17	...	n	...
5,6 ^a	1.62 ± 0.13	...	y	...

References. — (1) Hobbs 1974a; (2) Hobbs 1974b; (3) Hobbs 1976; (4) Stokes 1978; (5) Ferlet, Vidal-Madjar, & Gry 1985; (6) Herbig 1993.

Note. — Col.(1): Reference. Col. (2): Slope of conversion equation: $\log[N(\text{Na I})] = \beta \log[N(\text{H})] + \gamma$. Col. (3): Intercept of conversion equation. Col. (4): Is molecular hydrogen included in the calculation of the relation? y = yes [i.e. $N(\text{H}) = N(\text{H I}) + 2N(\text{H}_2)$]; n = no [i.e. $N(\text{H}) = N(\text{H I})$]; b = both (i.e. both kinds of data included). Col. (5): The ratio between $N(\text{H})$ determined using the conversion relationships in this table (“method 2”) and $N(\text{H})$ determined using the depletion correction from Savage & Sembach 1996 (-0.95) but with no ionization correction (“method 1”). The range of values is for the data in our sample. Note that we are able to compute $N_2(\text{H})$ for only those sources that include γ .

^aHerbig 1993 re-fitted the data of Ferlet et al. 1985, excluding cases where $N(\text{H})$ along a given sightline was subdivided into individual kinematic components and using values for $N(\text{Na I})$ from the earlier work of Hobbs where applicable.

Table 7. Host Galaxy Kinematics

IRAS FSC (1)	$\frac{1}{2}\text{FWHM}_{\text{avg}}^{\text{em}}$ (2)	$\frac{1}{2}\text{FWHM}_{\text{avg}}^{\text{abs}}$ (3)	σ_0 (4)	$\frac{1}{2}v_{\text{pp}}$ (5)	v_{rot} (6)	v_{esc} (7)
03250+1606	272	256	199	198	...	724
04313–1649	137	...	154	559
05024–1941	272	...	248	902
05189–2524	242	198	156	621
08559+1053	223	222	193	157	...	702
09039+0503	190	488
09116+0334	274	197	234	849
09539+0857	138	140	152	552
10190+1322:W	122	130	...	122	245 ^a	630
10190+1322:E	198	242	175	621
10378+1108	228	231	151	594
11387+4116	185	215	232	843
12540+5708	371

Note. — Col.(1): Target name. Col.(2): One-half the average FWHM of emission lines. Col.(3): One-half the average FWHM of Ca II triplet lines. Col.(4): Central velocity dispersion, computed from the R -band fundamental plane. Col.(5): One-half the peak-to-peak velocity amplitude determined from position-velocity diagrams. Col.(6): Rotation curve amplitudes from the Pa α line; from Murphy et al. 2001. Col.(7): Escape velocity, computed using a singular isothermal sphere with $r_{\text{max}}/r = 10$ and the maximum of $\frac{1}{2}\text{FWHM}_{\text{avg}}^{\text{em}}$, $\frac{1}{2}\text{FWHM}_{\text{avg}}^{\text{CaII}}$, $\sqrt{2}\sigma_0$, the rotation speed measured in position-velocity space, and, in the case of F10190 + 1322, the measured rotation speeds.

^aCorrected for a galaxy inclination of 40 – 50°.

Table 8. Emission Line Widths

IRAS FSC	[O III]	[O III]	[O I]	[N II]	H α	[N II]	[S II]	[S II]	avg
(1)	(2)	(3)	(4)	(5)	(6)	(7)	(8)	(9)	(10)
03250+1606	...	548:	484:	549	622	540	522:	...	544
04313–1649	294:	311:	284:	...	257	...	254	244	274
05024–1941	...	1167:	379:	...	682:	518:	240:	280:	544
05189–2524	768	821	260	...	441	...	299	312	483
08559+1053	521	324	552	...	356	392	489:	488	446
09039+0503	...	371	424	...	302	366	371	443	380
09116+0334	...	684:	483:	563	523	525	...	511	548
09539+0857	258:	251	253	341	255	291	275
10190+1322:W	...	255:	289:	287	184	212	245:	247	245
10190+1322:E	362:	317	507	399	397
10387+1108	510	432	467	416	456
11387+4116	...	305	405:	506	235	312	418	412	370

Note. — Col.(1): Target name. Col.(2)-(9): Full-widths at half-maximum of selected emission lines, in km s^{-1} . Uncertainties are generally 5 – 10%; numbers marked with a (:) have an uncertainty of 20%. Values have been corrected in quadrature for a finite instrumental resolution of 65 km s^{-1} . Wavelengths listed in the table header are wavelengths in air. Col.(10): Average FWHM.

Table 9. Absorption Line Widths

	H γ	H δ	H8	H9	H10	H11	H	Ca II K	Ca II	Ca II	Ca II	Ca II T
IRAS FSC	4340	4102	3889	3835	3798	3771	avg	3934	8498	8542	8662	avg
(1)	(2)	(3)	(4)	(5)	(6)	(7)	(8)	(9)	(10)	(11)	(12)	(13)
03250+1606	1807	1474	1187::	...	1489	1177	513::	513
04313-1649	1242::	1200	906	1051::	1100	490
05024-1941	865	...	1857	1277	975	...	1243	253
05189-2524	763	819	876	920	873	...	850	371	339	420	430	396
08559+1053	959	941	950	443	...	443
09039+0503	1289::	1216	664::	1056	819
09116+0334	...	1354	1404	1224	991	...	1243	...	347	441::	...	394
09539+0857	1860	1181	1088	...	1376	1018	...	260::	299	280
10190+1322:W	1589::	1072	927::	...	1196	472	224::	297	...	260
10190+1322:E	1336::	2012::	1674	582	...	483::	...	483
10378+1108	1221	1069	...	1145	999	392::	651::	343	462
11387+4116	...	1461	1777	1211	1011	...	1365	...	365	581	343::	430

Note. — Col.(1): Target name. Col.(2)-(7),(9)-(12): Full-widths at half-minimum of selected absorption lines, in km s^{-1} . Uncertainties are generally $\sim 20\%$; numbers marked with a (::) have an uncertainty of $\sim 40\%$. Values have been corrected in quadrature for a finite instrumental resolution of 65 km s^{-1} . Wavelengths listed in the table header are wavelengths in air. Col.(8): Average FWHM of Balmer lines. Col.(13): Average FWHM of Ca II triplet lines.

Table 10. Properties of Absorption Lines in Mrk 231

Δv	C_f	Na I D			He I $\lambda 3889$			Ca II H		
		$\tau_{1,c}$	b	N	τ_c	b	N	$\tau_{H,c}$	b	N
(1)	(2)	(3)	(4)	(5)	(6)	(7)	(8)	(9)	(10)	(11)
8062	0.2	0.16	141	0.80	0	0	0	0	0	0
6164	0.3	1.12	50	2.0	1.15	42	13	0	0	0
5500	0.3	1.43	41	2.1	0.72	17	3.3	0	0	0
5227	0.8	0.17	107	0.65	0.23	85	5.2	0.01	107	0.00
5015	0.5	1.01	118	4.3	1.50	115	46	0.31	120	1.9
4902	0.5	1.27	96	4.3	0.72	76	15	0.28	72	1.0
4766	0.7	1.01	47	1.7	0.80	35	7.5	0	0	0
4688	0.8	0.92	72	2.4	0.95	56	14	1.64	92	7.7
4563	0.9	0.86	83	2.5	0.59	131	20	0.62	85	2.7
4474	0.6	0.69	83	2.0	1.76	135	63	1.95	85	8.4
4383	0.7	1.96	48	3.4	0.19	46	2.3	0.26	142	1.9
4204	0.8	1.90	76	5.2	0.67	86	15	0.15	66	0.52

Note. — Col.(1): Velocity relative to systemic, in km s^{-1} : $\Delta v = v_{\text{sys}} - v$. Blueshifted velocities are positive. Col.(2): Covering fraction. Col.(3): Central optical depth of Na I D₁ $\lambda 5896$ line. Col.(4): Doppler parameter of Na I component, in km s^{-1} . Before conversion to b , the FWHM is corrected in quadrature for a 65 km s^{-1} instrumental resolution. Col.(5): Column density of Na I component, in units of 10^{13} cm^{-2} . Col.(6)-(8): Same as (3)-(5), but for He I $\lambda 3889$. Col.(9)-(11): Same as (3)-(5), but for Ca II H.